JCB Journal of Cell Biology

ARTICLE

An asymmetric junctional mechanoresponse coordinates mitotic rounding with epithelial integrity

Jooske L. Monster[1*], Lisa Donker[1*], Marjolein J. Vliem[1], Zaw Win[2], Helen K. Matthews[2], Joleen S. Cheah[3], Soichiro Yamada[3], Johan de Rooij[1], Buzz Baum[2], and Martijn Gloerich[1]

Epithelia are continuously self-renewed, but how epithelial integrity is maintained during the morphological changes that cells undergo in mitosis is not well understood. Here, we show that as epithelial cells round up when they enter mitosis, they exert tensile forces on neighboring cells. We find that mitotic cell–cell junctions withstand these tensile forces through the mechanosensitive recruitment of the actin-binding protein vinculin to cadherin-based adhesions. Surprisingly, vinculin that is recruited to mitotic junctions originates selectively from the neighbors of mitotic cells, resulting in an asymmetric composition of cadherin junctions. Inhibition of junctional vinculin recruitment in neighbors of mitotic cells results in junctional breakage and weakened epithelial barrier. Conversely, the absence of vinculin from the cadherin complex in mitotic cells is necessary to successfully undergo mitotic rounding. Our data thus identify an asymmetric mechanoresponse at cadherin adhesions during mitosis, which is essential to maintain epithelial integrity while at the same time enable the shape changes of mitotic cells.

Introduction

Epithelia cover the body surface and organs to form a regulated barrier between the internal and external environment. This barrier has to withstand the mechanical stresses to which epithelial cells are exposed, for instance, during morphogenetic movements (Takeichi, 2014; Lecuit and Yap, 2015). Integrity of the epithelial barrier depends on intercellular cohesion through adherens junctions, which are formed by homotypic interactions between E-cadherin proteins of adjacent cells. The cytosolic tail of E-cadherin associates with F-actin through β- and α-catenin, thereby coupling neighboring cells and their actomyosin cytoskeletons (Mège and Ishiyama, 2017). Moreover, the cadherin complex actively senses tensile forces between cells, which can trigger junctional reinforcement by recruitment of actin-modulating proteins that strengthen the cadherin-actin link (Leckband and de Rooij, 2014; Mège and Ishiyama, 2017; Charras and Yap, 2018). The best established among these is vinculin, which localizes to adherens junctions upon the tension-sensitive conformational opening of its binding site within α-catenin (le Duc et al., 2010; Yonemura et al., 2010; Thomas et al., 2013; Yao et al., 2014). Vinculin provides additional connections between the cadherin complex and actin and regulates local actin assembly (Leerberg et al., 2014; Ito et al., 2017), which can stiffen and strengthen cadherin adhesions (le Duc et al., 2010; Ladoux et al., 2010; Liu et al., 2010; Leckband et al., 2011). Force-induced vinculin recruitment to the cadherin complex has been implicated in tissue integrity (Huveneers et al., 2012); however, during which physiological processes this mechanoresponse is essential remains less well understood (Chen et al., 2018; Pannekoek et al., 2019).

The epithelial barrier is challenged by remodeling of the epithelium (Guillot and Lecuit, 2013), for instance, during homeostasis when apoptotic cell loss is continuously compensated by cell divisions (Blanpain et al., 2007). Following division, daughter cells form new cell–cell junctions, during which the integrity of the epithelial barrier is preserved (Higashi et al., 2016). Furthermore, cell division is accompanied by dramatic morphological changes, as cells round up in mitosis to ensure proper organization of the mitotic spindle (reviewed in Lancaster and Baum, 2014; Champion et al., 2017; Taubenberger et al., 2020). Mitotic rounding is initiated by dismantling of integrin-mediated cell-matrix adhesions to largely detach cells from their substrate (Yamakita et al., 1999; Dao et al., 2009; Marchesi et al., 2014). Cells then increase intracellular hydrostatic pressure (Stewart et al., 2011),

[1]Molecular Cancer Research, Center for Molecular Medicine, University Medical Center Utrecht, Utrecht, The Netherlands; [2]Medical Research Council Laboratory for Molecular Cell Biology, University College London, London, UK; [3]Department of Biomedical Engineering, University of California, Davis, Davis, CA.

*J.L. Monster and L. Donker contributed equally to this paper; Correspondence to Martijn Gloerich: m.gloerich@umcutrecht.nl.

which is accompanied by reorganization of the actomyosin network (Cramer and Mitchison, 1997; Maddox and Burridge, 2003; Matthews et al., 2012; Ramanathan et al., 2015). Together, this leads to the retraction of the cell margin to drive cellular rounding, and a concomitant increase in cortical stiffness (Cramer and Mitchison, 1997; Maddox and Burridge, 2003; Stewart et al., 2011; Matthews et al., 2012; Ramanathan et al., 2015; Sorce et al., 2015). Despite the morphological changes that occur following mitotic entry, cell–cell adhesions are preserved throughout the entire process of cell division (Baker and Garrod, 1993; Reinsch and Karsenti, 1994; Bauer et al., 1998). However, it is unclear to what extent mitotic rounding impacts cadherin junctions, and how the epithelial barrier is maintained during this process.

Here, we show that mitotic rounding imposes mechanical tension on neighboring cells, and that a vinculin-dependent mechanoresponse is required to maintain barrier integrity during mitotic entry. Surprisingly, we find that this mechanoresponse occurs asymmetrically at mitotic cell–cell junctions, as vinculin recruited to mitotic junctions originates selectively from neighbors of mitotic cells. Not only is this asymmetric junctional composition sufficient to reinforce mitotic cell–cell contacts, but our data also show that the absence of vinculin recruitment in mitotic cells is important to enable the concurrent actomyosin reorganization and changes in cell shape during mitotic entry.

Results

Mitotic rounding coincides with a local increase in epithelial tension

The morphological rearrangements that take place as cells enter mitosis have been well studied, predominantly in isolated, single cells (Taubenberger et al., 2020). However, how these mitotic shape changes impact the surrounding cells in epithelial tissues remains less well understood. To visualize this, we stably expressed the junctional protein GFP–α-catenin in Madin–Darby canine kidney (MDCK) epithelial cells. Live-cell imaging of MDCK monolayers showed the rounding of cells as they enter mitosis (Fig. 1, A and B; Fig. S1 A; and Video 1), which was accompanied by deformation of neighboring cells (Fig. 1 A and Video 1). Neighbors extend toward the mitotic cell, indicated by cellular strain in the direction of the mitotic cell (Fig. 1 C) and a concomitant increase in the length of their cell–cell contacts (Fig. 1, D and E). This cellular strain during mitotic rounding likely coincides with a local increase in mechanical tension in the epithelium. To test this, we used two-photon laser nanoscissors to cut the actin cortex at cell–cell contacts labeled with E-cadherin–DsRed and determined the recoil velocity following ablation as a measure of tension (Liang et al., 2016). This showed that the initial recoil was significantly faster at cell–cell contacts neighboring a mitotic cell compared with cell–cell contacts neighboring only interphase cells, indicating increased epithelial tension near mitotic cells (Fig. 1, F–H; Fig. S1 B; and Video 2). Altogether, these data imply that as cells enter mitosis and acquire their rounded morphology, they exert tensile forces on their neighbors.

An E-cadherin mechanoresponse triggers vinculin recruitment to mitotic cell–cell junctions

Tensile forces between cells are sensed by E-cadherin–based adhesions and can be transduced into an intracellular response to reinforce cell–cell adhesions, which involves the tension-sensitive recruitment of vinculin (Huveneers et al., 2012; le Duc et al., 2010; Yonemura et al., 2010; Thomas et al., 2009; Yao et al., 2014). To examine if tensile forces exerted by mitotic cells on surrounding cells induce this E-cadherin mechanoresponse, we monitored the localization of GFP-tagged vinculin. In confluent MDCK monolayers, GFP-vinculin localized to the cytosol and at focal adhesions, with low levels of vinculin at cell–cell contacts, as described previously (Fig. 2 A, Fig. S2 A, and Video 3; Ibar et al., 2018). Following entry into mitosis, we observed a strong increase in GFP-vinculin at cell–cell contacts, which was most prominent at tricellular junctions formed by mitotic cells and their neighbors (Fig. 2, A–C; and Video 3). Side-by-side analyses of cell morphology and junctional vinculin levels during mitotic progression demonstrated that the timing of junctional GFP-vinculin recruitment closely overlaps with cell rounding (Fig. 2 D). To ensure that the distribution of GFP-vinculin in our experiments was not obscured by the presence of endogenous vinculin, we monitored GFP-vinculin localization in vinculin knockout MDCK cells (Fig. S2, B and C). Importantly, while in these cells the localization of GFP-vinculin at interphase cell–cell junctions was more clearly visible, the strong enrichment of GFP-vinculin at cell–cell junctions following mitotic entry was present in these cells as well (Fig. S2 C and Video 4). Moreover, enrichment at mitotic cell–cell junctions could be validated for endogenous vinculin by immunostainings (Fig. 2 G). Accumulation at mitotic cell–cell junctions was not observed with unconjugated GFP or mScarlet controls (Fig. 2 E, Fig. S2 D, and Video 5). Finally, also in murine small intestinal organoids, which recapitulate the three-dimensional architecture of native epithelia, endogenous vinculin was enriched at cell–cell junctions of mitotic cells (Fig. S2, F–H).

To confirm that vinculin is truly enriched at cadherin- and not integrin-based adhesions in mitotic MDCK cells, we performed coimmunostainings of GFP-vinculin with E-cadherin and with the focal adhesion protein paxillin. This demonstrated the specific colocalization of vinculin with cadherin adhesions (Fig. S2 A). In line with this, junctional enrichment of vinculin in mitosis was completely lost in MDCK cells in which we replaced endogenous α-catenin with an α-catenin mutant in which the vinculin binding site (VBS) is mutated (α-catenin$^{\Delta VBS}$; Huveneers et al., 2012; Fig. 2, F and G). Junctional levels of GFP–α-catenin did not significantly increase in mitosis (Fig. S2 E and Video 1), indicating that vinculin enrichment is not a consequence of increased presence of α-catenin, but rather depends on the ability of α-catenin to bind vinculin.

Next, we set out to test whether the tensile forces exerted between mitotic cells and their neighbors are responsible for the recruitment of vinculin to mitotic cell–cell junctions. For this, we made use of MDCK cells in which endogenous cadherins are replaced by an N-terminally truncated E-cadherin mutant (E-cadherin^{T151}) that cannot form homotypic interactions and therefore does not transmit forces between cells (Troxell et al.,

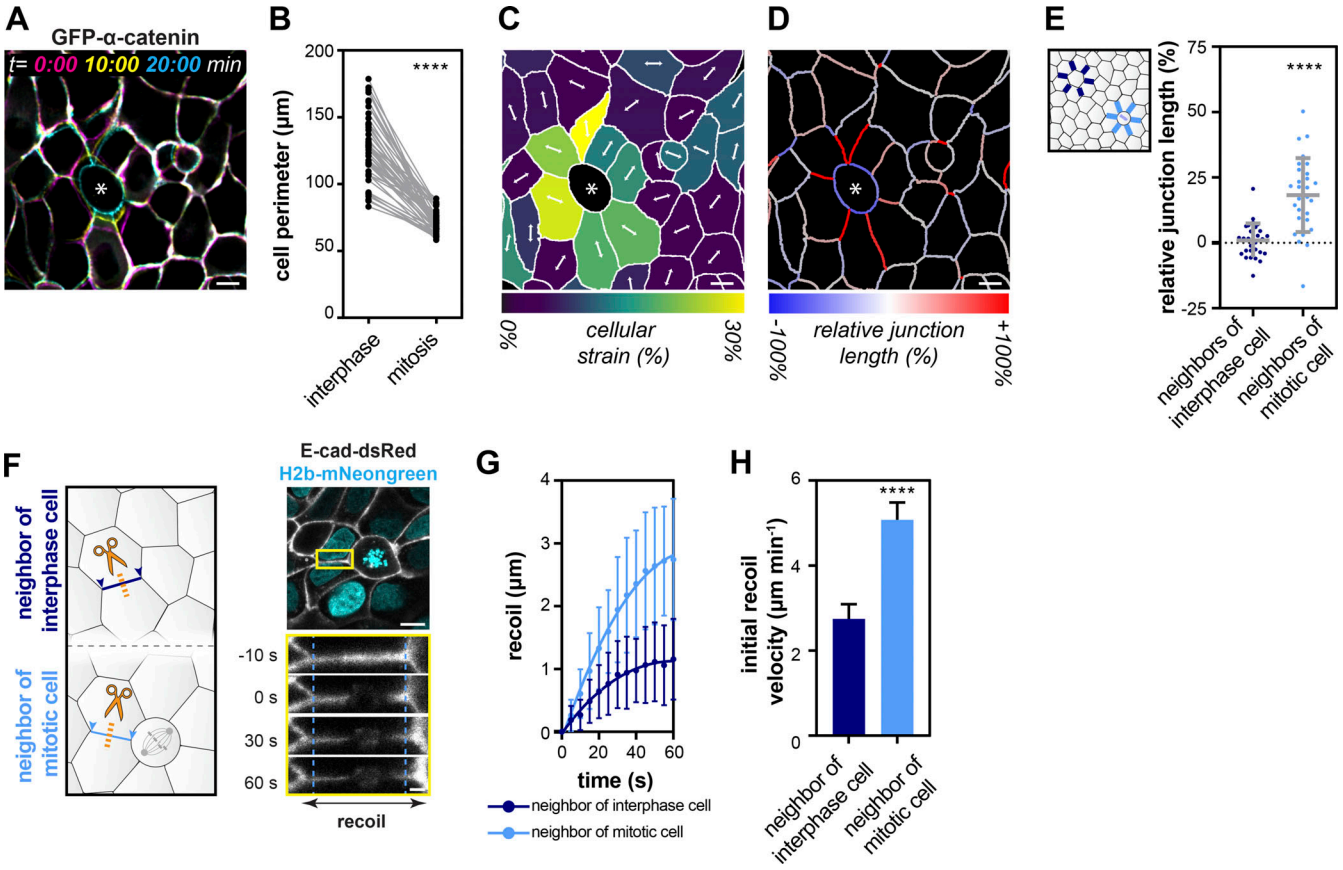

Figure 1. **Morphological changes in mitosis coincide with an increase in local tensile forces. (A)** Temporal color-coded overlay of an MDCK cell monolayer expressing GFP–α-catenin, with mitotic entry of a cell indicated by an asterisk (Video 1). **(B)** Quantification of cell perimeter of MDCK cells in interphase and following entry into mitosis. Quantified data were pooled from three independent experiments (n = 55). Gray bars show the mean cell perimeter with SD. ****, P < 0.0001; Wilcoxon matched-pairs signed-rank test. **(C)** Analysis of cellular (tensile) strain in an MDCK monolayer (A) as cells enter mitosis and undergo mitotic rounding over a period of 20 min. Cellular (tensile) strain is defined as the maximum relative increase in distance between two opposing cell edges (Δ length/initial length). The mitotic cell, which only undergoes compressive strain, is shown in black. The directionality of the maximum (tensile) strain is indicated by white arrows. **(D)** Analysis of the relative changes in junction length (Δ length/initial length) in an MDCK monolayer (A) as cells enter mitosis and undergo mitotic rounding over a period of 20 min. **(E)** Quantification of relative junction length (Δ junction length/initial junction length) in epithelial layers during progression from interphase to completion of mitotic rounding. Each dot represents the average change of length of all junctions neighboring either a mitotic cell (blue) or an interphase cell during the same time interval (dark blue; n = 29). Gray bars show the mean levels of change in length with SD. ****, P < 0.0001; Mann–Whitney. **(F)** Schematic illustration (left) of recoil analyses following nanoscissor laser ablation of the actin cortex at cell–cell contacts neighboring either interphase (dark blue) or mitotic (blue) cells. The representative example (right, Video 2) shows recoil of the cell–cell contact neighboring a mitotic cell (inset) over time. Note that nanoscissor ablation of the mitotic cell–cell junctions itself was not feasible, as mitotic cells immediately collapse following ablation (Fig. S1 C), which is likely explained by high osmotic pressure in mitotic cells (Stewart et al., 2011). **(G)** Quantification of the recoil of cell–cell contacts neighboring interphase (dark blue; n = 24) or mitotic (blue; n = 22) cells following laser ablation, defined as the absolute increase in distance between the two vertices of the ablated cell–cell contact (indicated by arrowheads in F). Dots represent the mean amount of recoil with SD, with lines showing the best-fit single exponential curve. Data were pooled from two independent experiments. Note that the differences in recoil between junctions neighboring mitotic and interphase cells were comparable when determined by the relative increase in distance between vertices (Fig. S1 B), indicating that changes in recoil in cell–cell contacts neighboring mitotic cells are not caused by differences in junctional length (E). **(H)** Initial recoil velocities for laser cuts of cell–cell contacts neighboring mitotic (n = 22) or interphase cells (n = 24). Bars show the average initial recoil velocities with SD. Data were pooled from two independent experiments. ****, P < 0.0001; unpaired t test. All scale bars, 10 μm or 2 μm (inset, F). E-cad, E-cadherin.

2000). Importantly, E-cadherin^{T151} retains an intact cytosolic tail that binds catenins, and cell–cell cohesion is maintained in E-cadherin^{T151} MDCK cells due to the presence of other types of cell–cell junctions (Fig. S2 I; Troxell et al., 2000). Cells expressing E-cadherin^{T151} no longer showed the enrichment of vinculin at cell–cell junctions upon mitotic rounding (Fig. S2 J), suggesting that this recruitment depends on E-cadherin force transmission between mitotic cells and their neighbors. To directly test whether mitotic enrichment of junctional vinculin is a result of tensile forces between mitotic and neighbor cells, we alleviated this tension using laser nanoscissors to cut the actin cortex of cell–cell contacts perpendicular to the mitotic cell (Fig. 2 H and Video 6). This led to a gradual decrease of GFP-vinculin on the associated tricellular junction (Fig. 2, H and I; and Video 6). In contrast, ablation did not affect GFP-vinculin levels at distant tricellular junctions of the mitotic cell (Fig. 2 H). Overall, these data indicate that tensile forces between mitotic cells and their neighbors induce an E-cadherin–dependent mechanoresponse and downstream vinculin recruitment to mitotic cell–cell junctions.

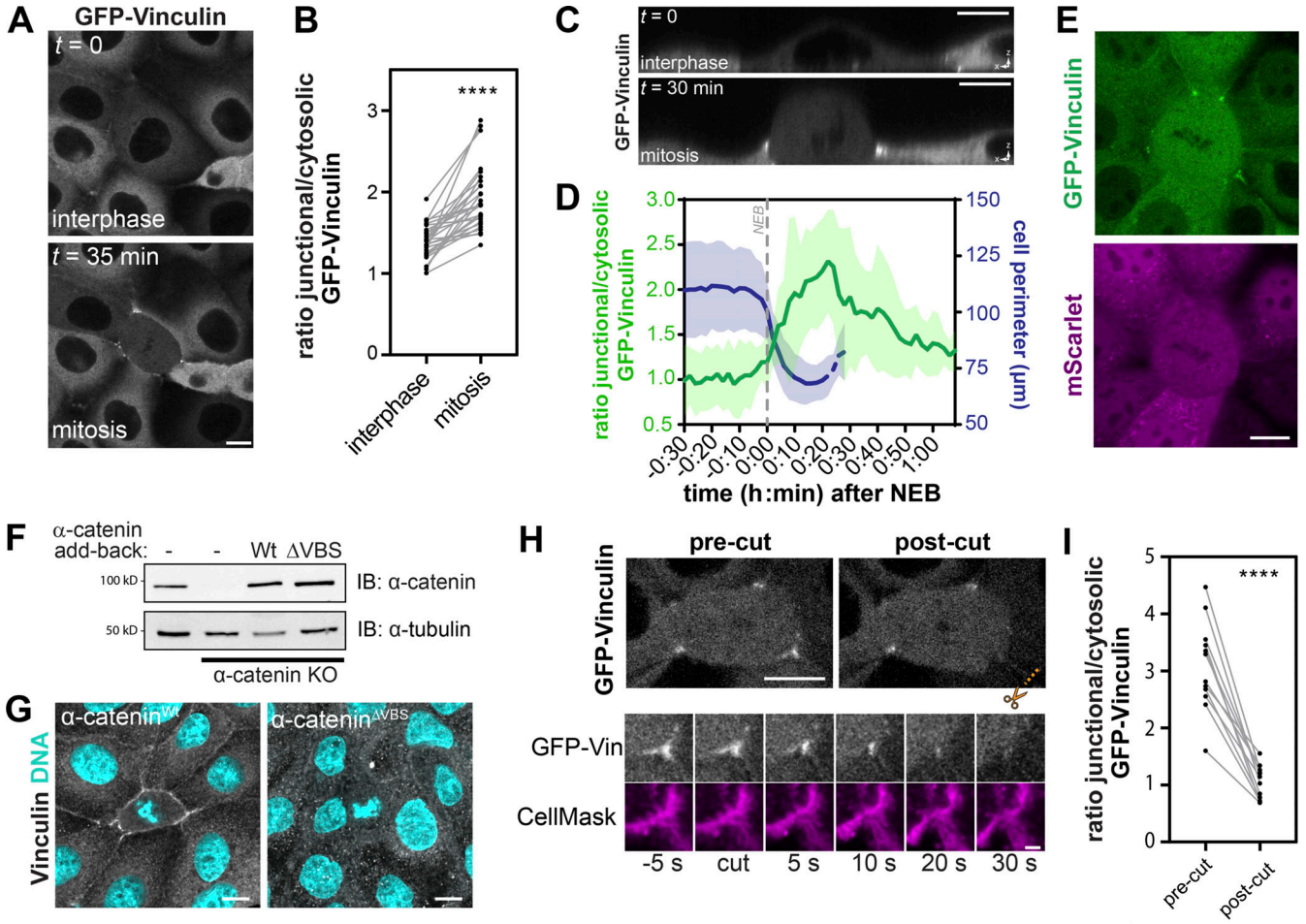

Figure 2. **Tension-sensitive recruitment of vinculin to adherens junctions during mitosis. (A)** Representative image (z-projection) of MDCK cells expressing GFP-vinculin in interphase and following entry in mitosis (Video 3). **(B)** Quantification of the ratio of junctional versus cytosolic GFP-vinculin in MDCK cells in interphase and following entry in mitosis (n = 27). Data were pooled from three independent experiments. ****, P < 0.0001; Wilcoxon matched-pairs signed-rank test. **(C)** Representative x,z-projection of MDCK cell expressing GFP-vinculin in interphase and following entry in mitosis. **(D)** Average cell perimeter ± SD (blue line) and the ratio of junctional versus cytosolic GFP-vinculin intensity ± SD (green line) during progression of cells through mitosis. Time-lapse images were aligned at the moment of nuclear envelope breakdown (NEB). Perimeter analyses were performed until the initiation of cytokinesis (dotted line represents average perimeter after measurement of first cell was completed). Note that the decrease in cell perimeter initiates shortly before NEB, in accordance with previous analyses of mitotic rounding in nonepithelial cells (Matthews et al., 2012). Data were pooled from three independent experiments (n = 9). **(E)** Representative image (z-projection) of mitotic MDCK cells coexpressing GFP-vinculin and unconjugated mScarlet. **(F)** Western blot of lysates from parental, α-catenin knockout (KO), and α-catenin KO with addback of WT- or vinculin-binding deficient (ΔVBS) α-catenin, MDCK cells probed for α-catenin and α-tubulin. **(G)** Immunostaining of MDCK cells (z-projection) expressing WT- or vinculin-binding deficient (ΔVBS) α-catenin for endogenous vinculin, together with DAPI. **(H)** Representative image of a mitotic MDCK cell expressing GFP-vinculin before and after laser ablation of the cortex of a cell–cell contact perpendicular to the mitotic cell (indicated with orange scissors; Video 6). The inset shows the tricellular junction associated with the ablated cell–cell contact over time. Note that the gradual decrease indicates that the disappearance of the GFP-vinculin signal is not due to bleaching during laser ablation of the junction, and that the tricellular junction itself remains intact as visualized by CellMask. **(I)** Quantification of the ratio of junctional versus cytosolic GFP-vinculin in mitotic MDCK cells before and after laser cuts (n = 12). Data were pooled from three independent experiments. ****, P < 0.0001; paired t test. All scale bars, 10 µm or 2 µm (inset, H). IB, immunoblot; t, time; Vin, vinculin.

The mitotic cadherin mechanoresponse is a direct consequence of mitotic cell rounding

Our data imply that mitotic rounding is directly responsible for elevated tensile forces between mitotic cells and their neighbors and the consequent mechanosensitive recruitment of vinculin to mitotic cell–cell junctions. We tested this by inhibition of contractility of the actomyosin network, which becomes enriched at the mitotic cell cortex (Fig. S3, A–C; and Video 7; Ramanathan et al., 2015) and drives mitotic rounding (Stewart et al., 2011; Ramanathan et al., 2015; Sorce et al., 2015). Upon chemical inhibition of actomyosin contraction or actin polymerization using blebbistatin or cytochalasin D, respectively (Fig. 3, A and B; and Video 8), both mitotic cell rounding and junctional GFP-vinculin enrichment upon mitotic entry were diminished (Fig. 3, A and B; and Video 8). As modulation of the actin cytoskeleton might affect junctional tension and vinculin recruitment independently of mitotic rounding, we next aimed to specifically inhibit mitotic rounding while leaving the actomyosin network intact. For this, we physically confined MDCK monolayers in height by positioning a polydimethylsiloxane (PDMS)-coated

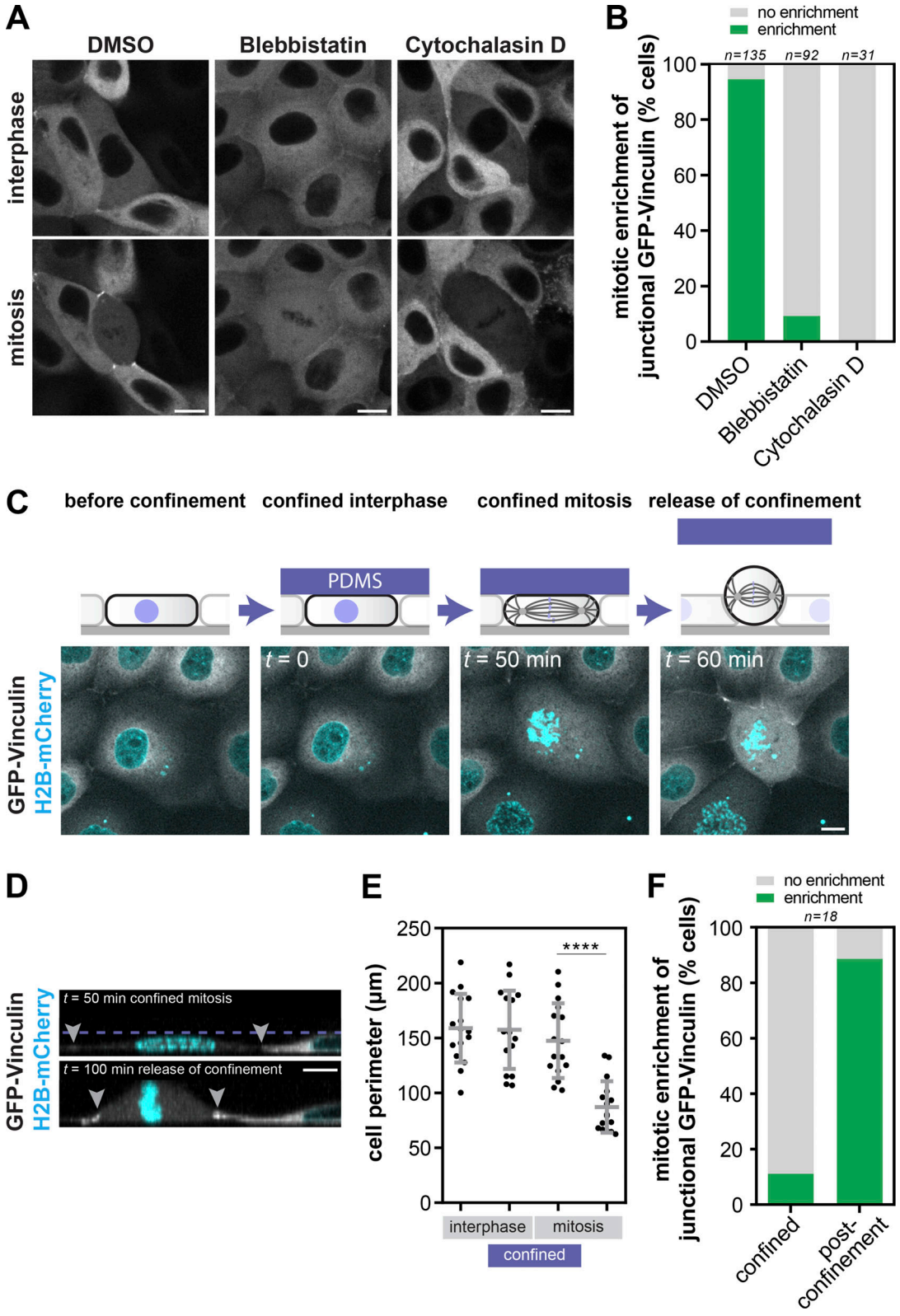

Figure 3. **The vinculin mechanoresponse is a direct consequence of mitotic rounding. (A)** Representative examples (z-projections) of MDCK cells expressing GFP-vinculin in interphase and following entry in mitosis in the presence of 10 µM para-nitro-blebbistatin, 2 µg/ml cytochalasin D, or DMSO control (Video 8). **(B)** Quantification of the fraction of mitotic cells with enrichment of junctional vinculin upon entry in mitosis in the presence of DMSO, para-nitro-blebbistatin, or cytochalasin D. Note that the small number of cells (8 out of 92) that still showed mitotic vinculin enrichment in the presence of blebbistatin also showed moderate mitotic rounding (not shown). Data were pooled from at least three independent experiments. DMSO versus blebbistatin: $P < 0.0001$; DMSO versus cytochalasin D: $P = 0.0028$; paired *t* test. **(C)** Top: Schematic diagram showing method of cellular confinement, in which MDCK cells are confined in height by a polydimethylsiloxane (PDMS)-coated glass slide during interphase to prevent rounding when cells enter mitosis. Bottom: Representative still

images (z-projections) of MDCK cells expressing GFP-vinculin and H2B-mCherry upon induction and release of confinement (Video 9). **(D)** Representative x,z-projection of a mitotic MDCK cell expressing GFP-vinculin and H2B-mCherry under confinement and following release of confinement. The locations of the cell–cell contacts are indicated with gray arrowheads, and the height of PDMS-coated glass slide (6 µm) is indicated by the purple dashed line. **(E)** Quantification of cell perimeter of cells upon induction and release of confinement (n = 16 cells). Gray bars show the mean cell perimeter with SD. Data were pooled from two independent experiments. ****, P < 0.0001; paired t test. **(F)** Quantification of the fraction of mitotic cells with enrichment of junctional vinculin following induction and release of confinement (n = 16). Data were pooled from two independent experiments. All scale bars, 10 µm.

glass slide on top of the epithelial layer, thereby confining the cells to 6 µm in height (Fig. 3, C and D; Le Berre et al., 2012; Lancaster et al., 2013). Whereas this confinement did not affect the shape of interphase cells, it successfully prevented cell rounding during mitosis (Fig. 3, C and E). Inhibition of mitotic rounding in confined epithelial monolayers prevented the mitotic enrichment of vinculin at cell–cell junctions (Fig. 3, C, D, and F; and Video 9). Upon release of confinement, mitotic cells rapidly proceeded to undergo rounding, which coincided with recruitment of GFP-vinculin to junctions (Fig. 3, C–F; and Video 9). These data indicate that mitotic rounding is directly responsible for the increased junctional tension that drives recruitment of vinculin to cell–cell contacts during mitotic entry.

Junctional vinculin recruitment during mitotic rounding is required for epithelial barrier function

The force-sensitive recruitment of vinculin to the cadherin complex regulates the organization of junctional actin, thereby reinforcing cell–cell adhesions to withstand intercellular stresses (Leckband and de Rooij, 2014; Pannekoek et al., 2019). We investigated whether the vinculin-dependent mechanoresponse is essential to preserve the integrity of cell–cell junctions following mitotic entry using our α-catenin$^{\Delta VBS}$ MDCK cells that cannot recruit vinculin to cell–cell junctions in mitosis (Fig. 2 G). Strikingly, in a large fraction of mitotic α-catenin$^{\Delta VBS}$ cells, we observed that cell–cell contacts were perturbed, resulting in the formation of gaps between mitotic cells and their neighbors (Fig. 4, A and B). No significant difference in junction integrity between cells expressing wildtype (WT) or ΔVBS α-catenin was observed during interphase (Fig. 4, A and B; and Fig. S4 A). This indicates that in unperturbed MDCK monolayers, the vinculin-dependent mechanoresponse at cadherin junctions is specifically required to maintain epithelial integrity during mitosis. To validate that the effect of α-catenin$^{\Delta VBS}$ is caused by disturbed vinculin function, we performed similar analysis of MDCK cells with shRNA-mediated depletion of vinculin. MDCK cells with reduced vinculin expression showed a similar loss of junctional integrity in mitotic cells, which could be restored by exogenous expression of WT vinculin (Figs. S4, B–D). Last, we tested if the vinculin-dependent mechanoresponse during mitosis is essential to maintain the barrier function of a polarized epithelium. MDCK cells expressing WT α-catenin were grown at high cell density on biotinylated Collagen IV until a functional epithelial barrier was formed that was impermeable to fluorescently labeled streptavidin added to the apical surface (Fig. 4, C and D; and Fig. S4 E). Under similar conditions, α-catenin$^{\Delta VBS}$ cells displayed barrier defects that occurred specifically during mitosis, as visualized by local permeability for streptavidin at cell–cell contacts of mitotic cells (Figs. 4, C and D). These data indicate that vinculin-dependent reinforcement of cell–cell junctions induced by an E-cadherin mechanoresponse is essential for junctions to withstand the increase in tensile forces induced by mitotic rounding and maintain junctional integrity and barrier function.

Recruitment of vinculin to cadherin occurs selectively in neighbors of mitotic cells

A vinculin-dependent mechanoresponse is expected to occur in both of the two neighboring cells forming a cell–cell junction that is under elevated tension. Indeed, upon elevation of junctional tension by incubation with HGF (le Duc et al., 2010), vinculin is recruited to cadherin adhesions in both cells forming the junction (Fig. S5 A). To visualize this in mitotic cells, we cocultured MDCK cells expressing either GFP- or mScarlet-tagged vinculin. Unexpectedly, using these mosaic cultures, we found that vinculin was essentially absent from the cell cortex within the mitotic cell, whereas at the same cell–cell junction, a clear enrichment of vinculin from the neighboring cell was observed (Fig. 5, A and B; and Fig. S5 B and Video 10). Importantly, mosaic cultures demonstrated that α-catenin remained present at the cell–cell contact in the mitotic cell, showing that junctional asymmetry is specific to vinculin (Fig. S5 C). These results reveal an asymmetric E-cadherin mechanoresponse upon mitotic rounding with vinculin specifically recruited to cadherin in the mitotic neighbor, whereas this enrichment of vinculin does not occur in the mitotic cell.

Our data suggest that epithelial barrier integrity depends on vinculin-mediated junctional reinforcement selectively in mitotic neighbors. To investigate this, we analyzed mosaic cultures of cells expressing WT and ΔVBS α-catenin, which are distinguished by expression of H2B-mCherry only in WT cells (indicated in magenta, Fig. 5 C). Strikingly, this showed that disruption of cell–cell contacts occurs specifically at sites where WT mitotic cells were adjoined by an interphase cell that expresses α-catenin$^{\Delta VBS}$ (Fig. 5, C and D). Conversely, in mitotic cells expressing α-catenin$^{\Delta VBS}$ that are adjoined by WT cells, cell–cell contacts remained unaffected (Fig. 5, C and D). These data demonstrate that vinculin is selectively recruited to the E-cadherin complex of cells neighboring a mitotic cell and not in the mitotic cell itself, and that this is sufficient to maintain junctional integrity during mitotic rounding.

Asymmetry in the recruitment of vinculin to mitotic cell–cell junctions enables mitotic rounding

As our results showed that the vinculin-dependent mechanoresponse occurs selectively in the neighbors of mitotic cells, we considered that the absence of this response in the mitotic cell itself could be imperative for successful mitotic progression. To

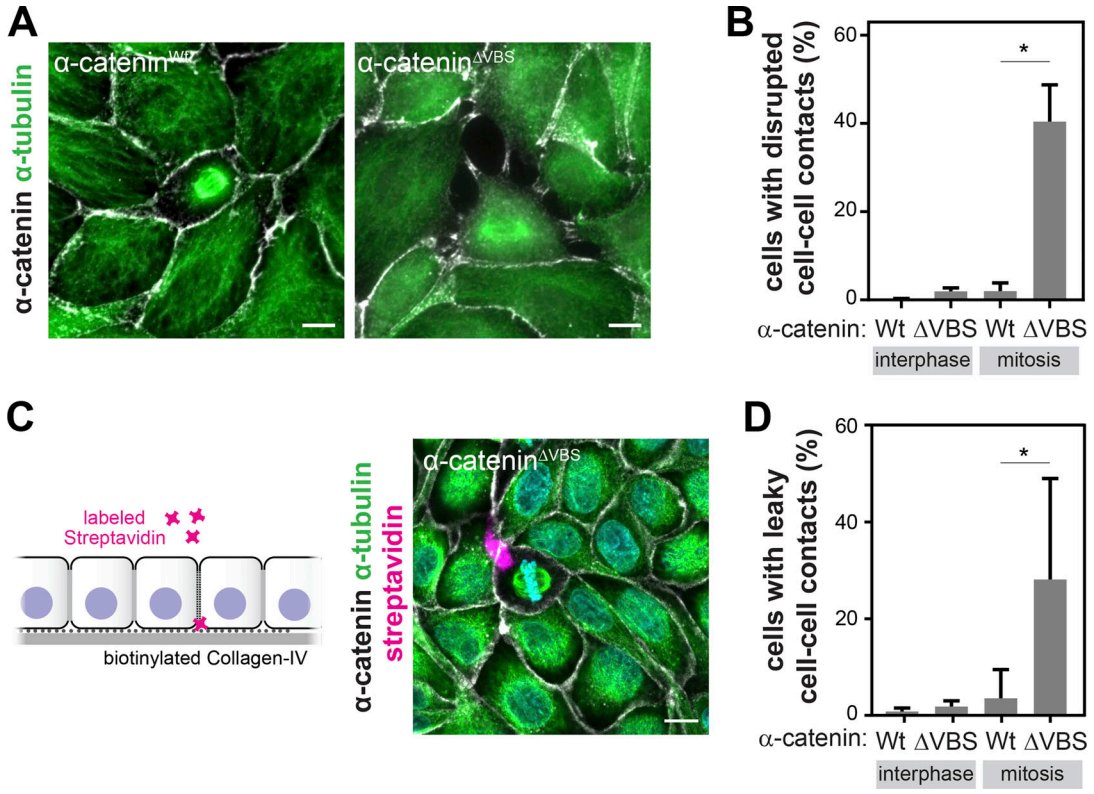

Figure 4. **Junctional vinculin recruitment during mitotic rounding is required for epithelial barrier function. (A)** Immunostainings of MDCK cells expressing WT- or vinculin- binding deficient (ΔVBS) α-catenin, for α-catenin and α-tubulin to visualize mitotic cells and the integrity of cell–cell contacts. **(B)** Quantification of the fraction of mitotic and interphase cells in which cell–cell contacts are perturbed, in WT and ΔVBS α-catenin MDCK monolayers. Data were pooled from three independent experiments, with at least 65 cells analyzed per condition in each experiment. Gray bars represent the mean and SD of the average fraction of disrupted cell–cell contacts in the independent experiments. *, $P < 0.02$; paired *t* test. **(C)** Left: Schematic representation of the permeability assay, in which streptavidin binds biotinylated Collagen IV at sites where the junctional barrier is perturbed. Right: Representative image of polarized MDCK cells (see Fig. S4 E) expressing α-catenin$^{\Delta VBS}$ incubated with labeled streptavidin (magenta), and following fixation immunostained for α-catenin and α-tubulin together with DAPI. **(D)** Quantification of the fraction of mitotic and interphase cells in which cell–cell contacts are permeable for streptavidin in WT and ΔVBS α-catenin expressing MDCK monolayers. Data were pooled from six independent experiments, with at least 30 cells analyzed per condition in each experiment. Gray bars represent the mean and SD of the average fraction of disrupted cell–cell contacts in the independent experiments. *, $P < 0.02$; paired *t* test. All scale bars, 10 µm.

investigate this, we aimed to artificially establish symmetry in vinculin distribution at mitotic cell–cell junctions. The lack of junctional vinculin recruitment in the mitotic cell could be explained by specific regulation of either vinculin or α-catenin that localizes vinculin to the cadherin complex. To discriminate between these possibilities, we made use of an α-catenin mutant that is constitutively in an open conformation, which enables binding of vinculin irrespective of upstream conformational regulation of α-catenin (M319G, R326E α-catenin; conformationally active [CA] α-catenin; Maki et al., 2016; Matsuzawa et al., 2018). In mosaic cultures with parental cells, expression of α-catenin^{CA} in mitotic cells (coexpressing GFP-vinculin) led to vinculin localization to the cadherin complex (Fig. 6, A and B; and Fig. S5 D). In contrast, expression of WT α-catenin did not result in enrichment of junctional GFP-vinculin in mitotic cells. This suggests that differences in the conformational state of α-catenin in the mitotic cell compared with its interphase neighbors prevent recruitment of vinculin, rather than distinct regulation of vinculin in the mitotic cell.

Next, we investigated whether progression through mitosis was affected when we forced the association of vinculin with the cadherin complex in the mitotic cell by α-catenin^{CA} expression. Strikingly, in cells expressing α-catenin^{CA}, we observed that mitotic rounding was strongly perturbed (Fig. 6 C). Quantification of mitotic cell shape showed that cells expressing α-catenin^{CA} did not acquire the same level of circularity as cells expressing α-catenin^{WT} (Fig. 6 D and Fig. S5 E). Moreover, mitotic cells expressing α-catenin^{CA} remained almost completely flat in mitosis compared with control cells (Fig. 6 E). As mitotic rounding relies on reorganization of the actomyosin cytoskeleton, we monitored the distribution of myosin IIA in cells expressing α-catenin^{CA} by immunostaining for T18,S19-phosphorylated myosin light chain 2 (pMLC). Whereas pMLC localized uniformly along the cell cortex of mitotic cells expressing WT α-catenin, in cells expressing α-catenin^{CA}, this localization was strongly perturbed (Fig. 6 F). pMLC displayed an irregular distribution at the cell cortex, and localized mainly at sites of cell–cell contacts instead of uniformly around the entire cell cortex (Fig. 6 F). This implies that the absence of junctional

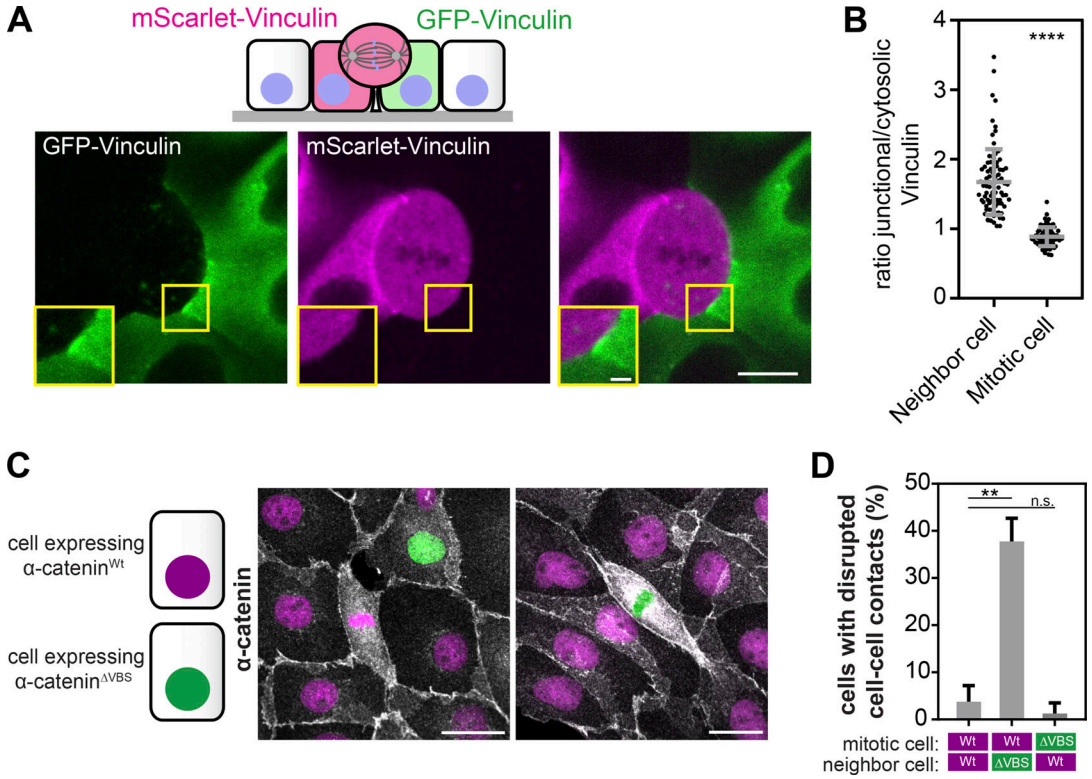

Figure 5. **A vinculin-dependent mechanoresponse occurs selectively in neighbors of mitotic cells. (A)** Top: schematic representation of coculture of MDCK cells expressing either GFP- or mScarlet-vinculin. Bottom: Representative image (z-projection) of a mitotic cell expressing mScarlet-vinculin with a neighbor expressing GFP-vinculin (Video 10). The inset (yellow) shows that the mitotic cell–cell contact contains a strong cortical GFP-vinculin enrichment originating from the neighboring cell, while mScarlet-vinculin is absent from the cortex of the mitotic cell. Similar results were obtained when the mitotic cell expressed GFP-vinculin and was adjoined by a neighbor expressing mScarlet-vinculin (Fig. S5 B). **(B)** Quantification of the ratio of junctional versus cytosolic vinculin intensity of mitotic cells and their interphase neighbors (n = 87 junctions). Gray bars show the mean ratio with SD. Data were pooled from three independent experiments, and from both mScarlet-vinculin mitotic cells with GFP-vinculin neighbors and vice versa, as no differences between the tags could be observed (see Fig. S5 B). ****, P < 0.0001; Wilcoxon matched-pairs signed-rank test. **(C)** Coculture of MDCK cells expressing either WT- or vinculin-binding deficient (ΔVBS) α-catenin, which are distinguished by expression of H2B-mCherry only in WT cells (all other nuclei are visualized with DAPI, shown in green). Left: Example of a mitotic cell expressing α-catenin^{WT} and neighbor expressing α-catenin$^{\Delta VBS}$. Right: Example of a mitotic cell expressing α-catenin$^{\Delta VBS}$ and neighbor expressing α-catenin^{WT}. **(D)** Quantification of the fraction of mitotic cells with disrupted cell–cell contacts in cocultures of MDCK cells expressing WT and ΔVBS α-catenin. Data were pooled from three independent experiments, with at least 10 cells analyzed per condition in each experiment. Gray bars represent the mean and SD of the average fraction of disrupted cell–cell contacts in the independent experiments. **, P = 0.02; paired t test; n.s., not significant (P = 0.45). All scale bars, 10 µm or 2 µm (inset, A).

vinculin in the mitotic cell enables remodeling of the actomyosin cytoskeleton and successful rounding during mitosis.

Discussion

Our results identify an asymmetric mechanoresponse at mitotic cell–cell junctions, which is essential to maintain epithelial integrity while enabling the concurrent changes in cell shape during mitotic entry (Fig. 7). These findings shed light on the regulation of the epithelial barrier during homeostasis, and provide novel insights into the regulation of E-cadherin junctions that can be of asymmetric nature.

We uncover force-dependent accumulation of vinculin at mitotic junctions that originates selectively from the neighbors of mitotic cells. Importantly, the cadherin–catenin complex itself is retained at the mitotic cell cortex of MDCK cells (Fig. S5 C). Asymmetry in junctional recruitment has been shown for curvature-sensing proteins, which recognize the convex-shaped membrane in cadherin-based protrusions that extend from migrating cells into their followers (Hayer et al., 2016; Dorland et al., 2016). However, components of the cadherin complex, including vinculin, retain a symmetric distribution between adjacent cells in these protrusions (Dorland et al., 2016). An important question for future investigations is how asymmetry in vinculin recruitment to mitotic cell–cell junctions arises. The absence of junctional vinculin recruitment is likely established by distinct regulation of α-catenin in the mitotic cell compared with its interphase neighbors, as an α-catenin mutant that is constitutively in an open conformation is able to localize vinculin to the mitotic cadherin complex (Fig. 6, A and B). A possible explanation for this could be that α-catenin in the mitotic cell may not be under sufficient tension to drive its open conformation. Although tensile forces are expected to be transmitted equally to both sides of adherens junctions, they could be transmitted to other components of the cell cortex rather than α-catenin in the mitotic cell. Alternatively, specific mechanisms

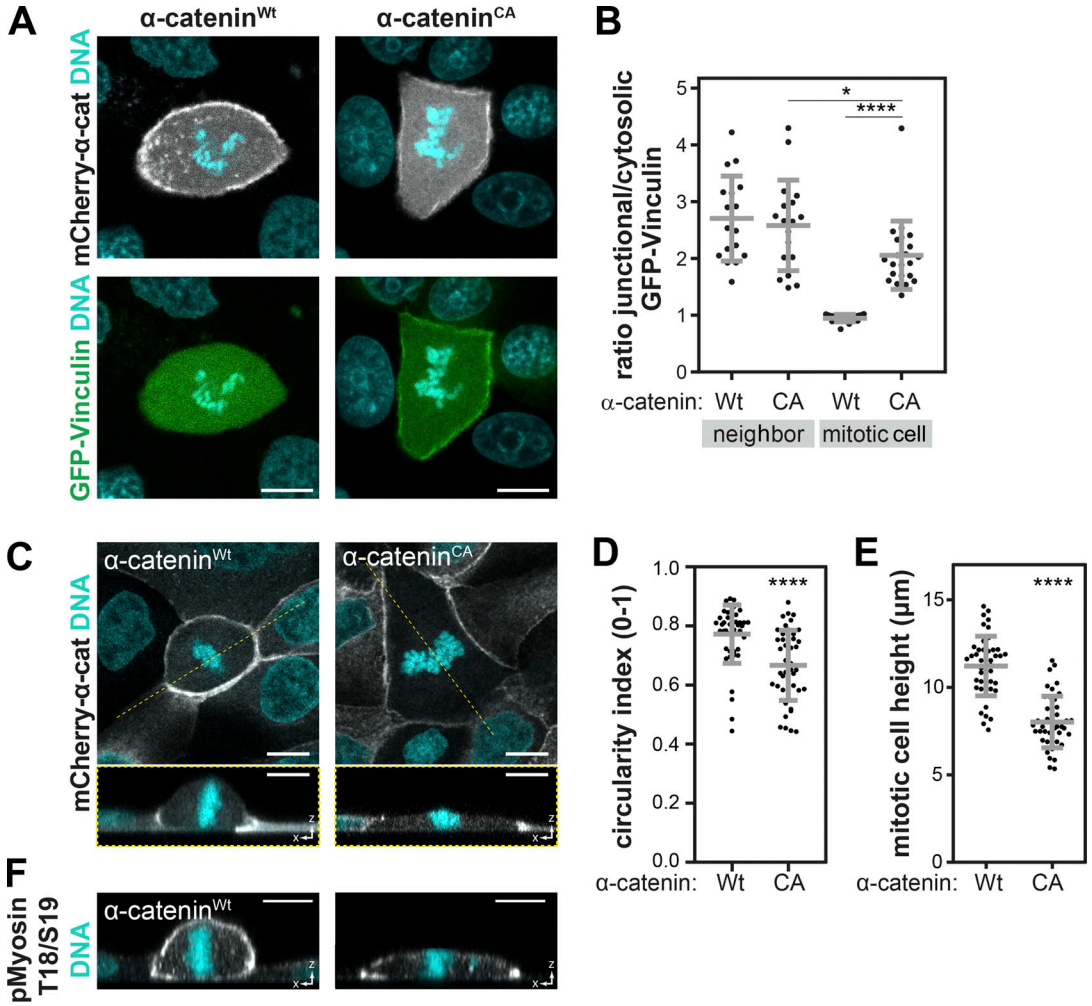

Figure 6. **Asymmetry in the recruitment of vinculin to mitotic cell–cell junctions enables mitotic rounding. (A)** Cocultures of parental MDCK cells, with cells inducibly expressing either mCherry–α-catenin^{WT} (left) or mCherry–α-catenin$^{M319G,\ R326E}$ (α-catenin^{CA}; right) together with GFP-vinculin. Shown are representative examples (z-projections) of mitotic cells expressing mCherry–α-catenin, surrounded by parental MDCK cells. Nuclei are visualized with Hoechst. **(B)** Quantification of the ratio of junctional versus cytosolic GFP-vinculin intensity in mitotic cells, and interphase neighbors of mitotic cells, expressing either WT- or CA mCherry–α-catenin (n = 17, 18, 21, and 22, respectively). Gray bars show the mean ratio with SD. Note that the ratio of junctional/cytosolic GFP-vinculin in mCherry–α-catenin^{CA}—expressing cells is significantly less in mitotic cells compared with interphase neighbors, which is due to the increase in cytosolic vinculin intensity in mitotic cells compared with interphase cells. Data were pooled from four independent experiments. *, P = 0.0189; ****, P < 0.0001; Mann–Whitney. **(C)** Monolayers of MDCK cells expressing WT or CA mCherry–α-catenin, with representative examples of x,y- and x,z-projections of mitotic cells in metaphase. The dashed line indicates the position of the shown x,z-projection. **(D and E)** Quantifications of the (D) circularity (4π × area/perimeter^2) and (E) height of MDCK cells in metaphase expressing either WT- or CA α-catenin (n = 45 per condition). Gray bars show the mean cell circularity or height with SD. Note that these differences are not attributed to a delay in rounding, as the kinetics of mitotic rounding were unaffected in α-catenin^{CA} cells (Fig. S5 F). Quantified data were pooled from three independent experiments. ****, P < 0.0001; Mann–Whitney. **(F)** Representative x,z-projections of mitotic MDCK cells expressing WT- or CA α-catenin, immunostained for pMLC. Nuclei were stained with DAPI. All scale bars, 10 µm. α-cat, α-catenin.

may be present in mitotic cells that regulate the conformational state of α-catenin and/or its ability to bind vinculin, for instance, mitosis-specific competing interactors or post-translational modification of α-catenin. Notably, several phosphorylation events on α-catenin have been identified to be regulated during mitosis (Daub et al., 2008; Olsen et al., 2010); however, these are within regions of α-catenin that would not likely influence its conformation or vinculin binding directly.

Our data show that the asymmetric junctional composition is sufficient to reinforce mitotic cell–cell contacts, and moreover, that the absence of cortical vinculin is essential to enable the concurrent changes in cell shape during mitotic entry. Why it is essential that the mechanoresponse at mitotic junctions is asymmetric may be explained by the regulation of the actomyosin network in mitotic cells. During interphase, cell–cell adhesions form the predominant sites for connections of cortical actomyosin to the lateral membrane in epithelial cells (Bachir et al., 2017). The changes in cell shape during mitotic entry rely on reorganization of actomyosin into an isotropic network along the entire cell cortex, which is connected to the plasma membrane via ERM-family proteins (Carreno et al., 2008; Kunda et al., 2008; Matthews et al., 2012; Ramanathan et al., 2015; Rosa et al., 2015). Destabilizing the connection of the actin cytoskeleton with cadherin junctions may be needed to ensure this

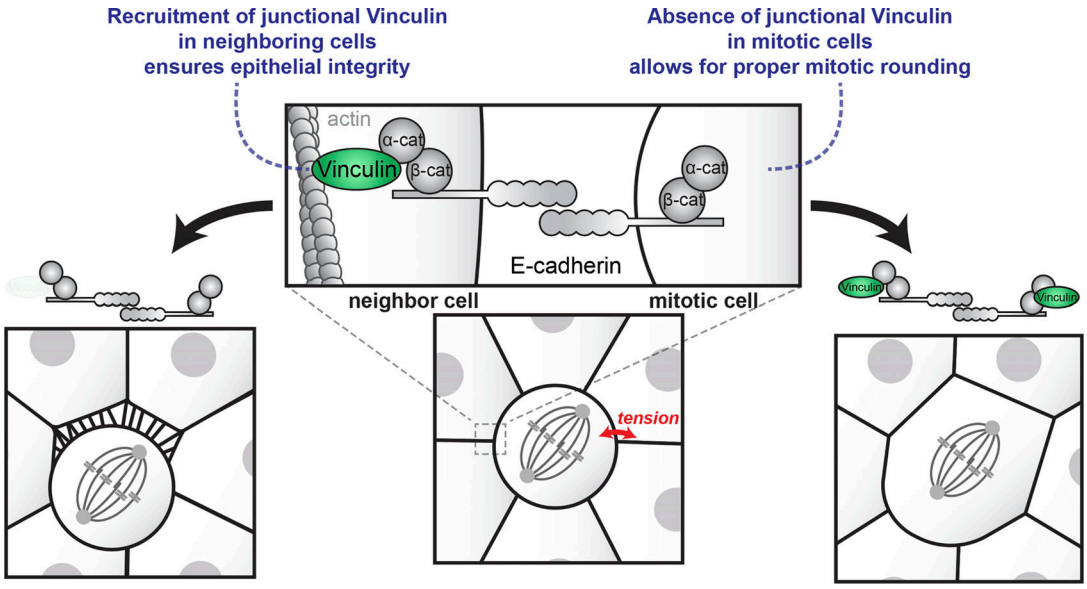

Figure 7. **Summary of the identified asymmetric E-cadherin mechanoresponse during mitosis.** Mitotic rounding increases tensile forces on adhesions between mitotic cells and their neighbors, resulting in accumulation of vinculin at mitotic junctions that originates selectively from cells neighboring the mitotic cell. This mechanoresponse in the mitotic neighbors is sufficient to reinforce mitotic junctions and maintain epithelial integrity, while the absence of junctional vinculin recruitment in the mitotic cell is essential for cells to successfully undergo mitotic rounding. cat, catenin.

uniform actomyosin distribution. This could explain why the absence of vinculin from the mitotic cadherin complex, which would otherwise reinforce the cadherin-actin link, is essential to enable mitotic rounding. In line with this, when vinculin is forced to the cadherin complex in mitotic cells by α-catenin^{CA} expression, the uniform distribution of myosin IIA is perturbed and displays an irregular distribution at the mitotic cell cortex with predominant localization at sites of cell–cell contacts (Fig. 6 F). The reorganization of the actomyosin network in mitosis may also explain why a vinculin-dependent mechanoresponse in mitotic neighbor cells is sufficient to reinforce junctions. Actomyosin remodeling induces stiffening of the cortex of mitotic cells (Kunda et al., 2008; Matthews et al., 2012), which may help to promote resistance of the mitotic cell cortex to intercellular stresses.

In addition to vinculin, α-catenin can recruit other actin-binding proteins (e.g., afadin; Sawyer et al., 2009; Matsuzawa et al., 2018) and binds F-actin directly through a catch-bond interaction (Buckley et al., 2014; Ishiyama et al., 2018). It will be interesting to explore to what extent these alternative connections between the cadherin complex and actin network are regulated in mitotic cells. Importantly, alternative actin-associated proteins recruited to α-catenin may act redundantly with vinculin in reinforcing mitotic cell–cell junctions, which could explain the relatively mild phenotype of selectively losing vinculin in flies (Alatortsev et al., 1997).

We demonstrate that increased junctional tension and concomitant vinculin recruitment are a direct consequence of mitotic rounding, a universal process that occurs in epithelial tissues throughout the Metazoa (Lancaster and Baum, 2014; Champion et al., 2017). We found vinculin to be enriched at mitotic cell–cell junctions in MDCK cells as well as small intestinal organoids that recapitulate the three-dimensional architecture of native epithelia (Fig. S2, F–H). Moreover, it was recently shown that during blastocyst development, elevated luminal pressure induces junctional rupture specifically when cells enter mitosis (Chan et al., 2019), which supports our data that mitotic rounding imposes an increased level of stresses on junctions. Similarly, genetically disrupting the link between cadherin junctions and actin results in rupture of cell–cell contacts in the dorsal ectoderm of the *Drosophila melanogaster* embryo when cells enter mitosis (Manning et al., 2019). It will be interesting to test how different properties of the epithelium may influence mechanical stresses during mitosis and the induction of the mitotic E-cadherin mechanoresponse. For instance, in certain epithelial tissues such as in the *Xenopus laevis* embryo, cells do not undergo rounding during mitosis, which likely explains why a cadherin mechanoresponse is absent in these cells during mitotic entry (Higashi et al., 2016; Herbomel et al., 2017). Moreover, while epithelia require constant maintenance of the epithelial barrier, recent findings show that in mesenchymal deep cells of the zebrafish blastoderm cell–cell junctions are weakened in mitosis to drive tissue fluidization (Petridou et al., 2019). Future studies may answer whether a cadherin mechanoresponse can be adjusted to establish distinct regulation of mitotic junctions in different tissues.

Materials and methods

Antibodies and reagents

The following commercial antibodies were used at the indicated concentrations for Western blot (WB) and immunofluorescence (IF): mouse anti-vinculin (hVIN-1; Sigma-Aldrich; V9131; 1:250 IF; 1:2,500 WB), mouse anti-α-tubulin (DM1A; Sigma-Aldrich; T6199; 1:1,000 IF), mouse anti-α-tubulin (B-5-2-1; Sigma-Aldrich; T5168; 1:10,000 WB), mouse anti-paxillin (clone 349;

BD Biosciences; 610052; 1:500 IF), rabbit anti-pMLC (Cell Signaling; 3674; 1:250 IF), rat anti-E-cadherin (DECMA-1; GeneTex; GTX11512; 1:1,000 IF), rabbit anti-αE-catenin (Sigma-Aldrich; C2081; 1:500 IF), mouse anti-αE-catenin (Enzo; ALX-804-101-C100; 1:2,500 WB), and mouse anti-ZO-1 (1A12; Life Technologies; 33–9100; 1:500 IF). The following reagents were used at the indicated concentrations: para-nitro-blebbistatin (Opto-Pharma Ltd.; DR-N-111; 10 µM), cytochalasin D (Sigma-Aldrich; C8273; 2 µg/ml) and HGF (R&D Systems; 294-HGN; 15 ng/ml). CellMask Deep Red Plasma membrane Stain (Thermo Fisher Scientific; C10046) and SiR-actin (SpiroChrome; CY-SC001) were used where indicated and according to the manufacturer's protocol.

Plasmids

The following plasmids are described elsewhere: pCDNA3 EGFP-CAAX (kind gift from Kees Jalink, Netherlands Cancer Institute, Amsterdam, The Netherlands; van der Wal et al., 2001), pLV-CMV-IRES-Puro plasmid containing WT or ΔVBS αE-catenin (Twiss et al., 2012), pLV-CMV-IRES-Puro H2B-mNeongreen (Drost et al., 2015), pLV-CMV-IRES-Puro mCherry-αE-catenin (GenInfo Identifeir [GI]: 49935; Oldenburg et al., 2015) and pWPT-hEF1α-H2B-mCherry (kind gift from Susanne Lens, University Medical Center Utrecht, Utrecht, The Netherlands; Adriaans et al., 2019). Additional plasmids were generated using In-Fusion Cloning: pLV-CMV-IRES-Puro mScarlet-I (inserting mScarlet-I [Bindels et al., 2017] in pLV-CMV-IRES-Puro), mScarlet-I-vinculin-C1 [*Gallus gallus*; GI: 396422; replacing EGFP of EGFP-vinculin-C1 [Yamada et al., 2005] with mScarlet-I, including a 20–amino acid linker SGLRSRAQASNSGPPCPAAA), and pInducer20 mCherry-αE-catenin (inserting mCherry-αE-catenin [GI: 49935; Oldenburg et al., 2015] in pInducer20 vector [Addgene; #44012]). Finally, M319G, R326E αE-catenin (α-catenin^{CA}; Matsuzawa et al., 2018) mutants were created in both pLV-CMV-IRES-Puro plasmid and pInducer20 plasmids using PCR mutagenesis.

Cell lines and culture

MDCK GII cells were cultured at 37°C and 5% CO_2 in low-glucose DMEM containing 10% FBS, 1 g/liter sodium bicarbonate, and penicillin/streptomycin. Live-cell imaging was performed with the same media formulations in the absence of phenol red. MDCK αE-catenin knockout cells (Ortega et al., 2017) and MDCK cells stably expressing GFP–αE-catenin (Yamada et al., 2005), E-cadherin–DsRed (Yamada et al., 2005), GFP-vinculin (Yamada et al., 2005), E-cadherin^{T151} (Troxell et al., 2000), vinculin shRNA (Sumida et al., 2011), or GFP-myosin IIA (Jorrisch et al., 2013) were described previously. MDCK cells expressing vinculin shRNA rescued with WT mCherry-vinculin were a kind gift from Brenton Hoffmann (Duke University, Durham, NC). Additional stable MDCK cell lines were generated using transfection reagent Lipofectamine 3000 (Thermo Fisher Scientific) or by lentiviral transductions. Vinculin knockout lines were generated by stably expressing a PiggyBac plasmid encoding a cumate-inducible Cas9 and a canine vinculin–specific gRNA (5′-GGAGCACCGAGTAATGTTGG-3′). Homozygous knockout lines were verified both by PCR-amplifying the target sequences from genomic DNA of knockout cell lines and insertion into TOPO vectors (Invitrogen) for sequencing, and by WB (Fig. S2 B). For cells with doxycycline-induced α-catenin expression (Fig. 6), cells were cultured in medium containing 2 µg/ml doxycycline for at least 24 h; E-cadherin^{T151} cells were cultured in the absence of doxycycline for at least 2 wk. All cell lines were regularly tested for the absence of mycoplasma.

Cell microscopy and analyses

For live-cell imaging, cells were seeded on glass-bottom dishes (WillCo-dish or Lab-Tek II) precoated with Rat Tail Collagen I (Corning), and imaged on a Zeiss Cell Observer equipped with Orca Flash 4.0 camera (Hamamatsu) using a 63× objective (NA = 1.3; Fig. S3 A), on a Zeiss LSM880 scanning confocal microscope using a 63× objective (NA = 1.15; Figs. 6 A, S4 E, and S5 D), or on a Nikon Spinning Disc confocal microscope using a 60× objective (NA = 1.49; Fig. 1 A; Fig. 2, A, C, and E; Fig. 3 A; Fig. 5 A; Fig. S2, C–E; and Fig. S5, A–C). Imaging was performed at 37 C° and 5% CO_2 in temperature- and CO_2-controlled incubators, using Zen image acquisition software and NIS-Elements software, respectively.

For cell morphology analysis, MDCK cells were imaged with a time interval of 10–15 min, and cell perimeter and circularity were measured in interphase (10–15 min before nuclear envelope breakdown) and in metaphase, using ImageJ software (National Institutes of Health) and the BioVoxxel plugin (Fig. 1 B; Fig. 2, D–G; and Fig. S1 A). The ratio of junctional/cytosolic distribution of GFP-vinculin (Fig. 2, B, D, and H; Fig. 5 B; Fig. S2 C; and Fig. S5 B), mScarlet-vinculin (Figs. 5 B and S5 B), GFP (Fig. S2 D), and GFP–α-catenin (Fig. S2 E) was calculated from the average fluorescence intensity at tricellular junctions relative to the intensity in the cytosol of the two neighboring cells using circular regions of interest with 4-pixel diameter in ImageJ, either for individual tricellular junctions (Fig. 2, D and H; Fig. 5 B; and Fig. S5 B) or the average of all tricellular junctions of each cell (Fig. 2 B; and Fig. S2, D and E). All analyses were performed on maximum projections of z-stacks. The cellular distributions of GFP-vinculin and myosin IIA in Figs. S3 B and 6 B were quantified using line scan analysis in ImageJ. The ratio of cortical/cytosolic distribution was calculated from the average fluorescence intensity at cell–cell contacts relative to the intensity in the cytosol of the neighboring cell, based on 10 randomly positioned line scans (pixel width 10) for each cell. For actomyosin manipulations, cells were treated with cytochalasin D and para-nitro-blebbistatin for at least 10 and 30 min, respectively, before the GFP-vinculin enrichment upon mitotic entry was assessed (Fig. 3, A and B). Cells were imaged and included for analyses in an unbiased manner. Only mitotic cells that also had mitotic neighbors were excluded from the analyses.

For IF stainings, cells were fixed with 4% formaldehyde (Sigma-Aldrich); permeabilized with 0.2% Triton X-100 (Sigma-Aldrich); blocked in buffer containing 1% BSA (Sigma-Aldrich), 1% goat serum (Life Technologies), and 1% donkey serum (Jackson Immunoresearch); and incubated with the indicated primary and Alexa-conjugated secondary antibodies (Life Technologies), together with DAPI (Sigma-Aldrich) where indicated. Cells were analyzed on a Zeiss LSM880 scanning confocal microscope using a 40× objective (NA = 1.1; Fig. S2 I) or 63×

objective (NA = 1.15), with the exception of Fig. 4, A and C; and Fig. S4 C, which were analyzed on a Zeiss Cell Observer equipped with Orca Flash 4.0 camera (Hamamatsu) with a 63× objective (NA = 1.3), using Zen image acquisition software. For analysis of the integrity of cell–cell contacts in cells in interphase and mitosis (metaphase), disrupted cell–cell contacts were visualized by α-catenin staining. For mitotic cell shape analyses of fixed cells (Fig. 6, D and E; and Fig. S5 E), circularity, perimeter, and height were measured in metaphase cells using ImageJ software (National Institutes of Health) and the BioVoxxel plugin. Cells were imaged and included for analyses in an unbiased manner. Only mitotic cells that also had mitotic neighbors were excluded from the analyses.

Strain analyses

The maximum cellular (tensile) strain was measured in MDCK cells expressing GFP–α-catenin live-imaged with a 10-min time interval. For this, we measured the maximal change in distance between two opposite cell borders in two frames to calculate cellular strain (Δlength/initial length) using ImageJ. To determine junctional strain, MDCK cells expressing GFP–α-catenin, live-imaged with a 10-min time interval, were segmented based on watershed using the Python script SeedWaterSegmenter (Mashburn et al., 2012), and junction length analysis was performed using custom Python scripts in Spyder. Junctional strain in mitotic neighbors was determined by calculating the lengths of junctions perpendicular to mitotic cells in interphase and metaphase (Δlength/initial length; 20–30-min difference). Interphase cells were selected within the same frame as the mitotic cell, with a distance of at least two cells from a mitotic cell. For the quantification (Fig. 1 E), all neighboring junctions of one mitotic or interphase cell were averaged.

Intestinal organoid culture and immunostaining

Small intestinal organoids, derived from isolated crypts collected from the entire length of the small intestine of WT mice (Sato et al., 2009), were cultured at 37°C and 5% CO_2 in Matrigel (Corning) in advanced DMEM/F12 medium (Invitrogen) containing 1% GlutaMax (Invitrogen), 0.01 M Hepes buffer (Life Technologies) and 1% penicillin/streptomycin (Lonza), supplemented with 1× B27 (Invitrogen), 1.25 mM n-acetyl cysteine (Sigma-Aldrich), 50 ng/ml recombinant mEGF (Peprotech), R-Spondin1–conditioned medium (5% vol/vol), and Noggin-conditioned medium (10% vol/vol). For immunostainings, organoids were mechanically dissociated and seeded in Matrigel on glass-bottom dishes (WillCo-dish), and following 4–5 d of culture, fixed in 4% formaldehyde (Thermo Fisher Scientific), permeabilized in buffer containing 1% BSA (Sigma-Aldrich), 10% DMSO (VWR Chemicals), and 2% Triton X-100 (Sigma-Aldrich) in PBS, and incubated with the indicated primary and Alexa-conjugated secondary antibodies (Life Technologies) together with DAPI for at least 16 h, all at 4°C. Imaging was performed on a Zeiss LSM880 scanning confocal microscope with a 40× objective (NA = 1.1) using Zen image acquisition software (Fig. S2 F). The cellular distribution of vinculin (Fig. S2, G and H) was quantified using line scan analysis in ImageJ (National Institutes of Health), and the ratio of junctional/cytosolic distribution was calculated from the average fluorescence intensity at cell–cell contacts (visualized by α- or β-catenin staining) relative to the intensity in the cytosol of the neighboring cell, based on three randomly positioned line scans (pixel width 10) for each cell. In addition, the ratio of the intensity of vinculin at cell–cell contacts relative to the intensity the junctional marker (α-catenin or β-catenin) was quantified.

Laser ablation experiments

For nanoscissor laser ablation experiments, cells were seeded on glass-bottom dishes (Lab-Tek II) precoated with Rat Tail Collagen I (Corning), and imaged with a 2–5-s time interval on a Zeiss LSM880 scanning confocal microscope using a 63× objective (NA = 1.15) at 37 C° and 5% CO_2 in a temperature- and CO_2-controlled incubator. Cell–cell contacts were visualized by E-cadherin–DsRed expression or by CellMask (Thermo Fisher Scientific) as indicated, and ablated by 30 iterations at a consistently sized region of interest with a 790-nm Ti Sapphire laser (Chameleon Ultra; Coherent Scientific). For determining recoil velocity, distances (d) between vertices of the ablated cell–cell contacts prior to ($d(0)$) and following ablation ($d(t)$) were determined using ImageJ software and plotted as a function of time ($f(t)$) using Prism 8 software (GraphPad). Initial recoil velocities, as well as the ratio between junctional elasticity and viscosity of the media (k), were computed as described previously (Liang et al., 2016; Teo et al., 2020) by nonlinear regression of the data to the following equation:

$$d(t) - d(0) = f(t) = \frac{initial\ recoil}{k}(1 - e^{-kt})$$

For determining the localization of GFP-vinculin after alleviation of tension by laser ablation, we in addition imaged z-stacks of the entire monolayer prior to and following laser ablation, and analyses of GFP-vinculin distribution were performed on maximum projections of z-stacks as described above.

Streptavidin permeability assay

MDCK αE-catenin knockout cells expressing WT or ΔVBS αE-catenin were seeded on glass-bottom dishes (Lab-Tek II; Thermo Fisher Scientific) coated with 5 mg/ml Collagen IV (C5533; Sigma-Aldrich) that was biotinylated using NHS-LC-Biotin (EZ-Link; Thermo Fisher Scientific), according to the manufacturer's protocol. Cells were cultured until a polarized epithelium was formed (as indicated by formation of an apical brush border), and 25 µg/ml streptavidin conjugated with Alexa Fluor 568 (S11226; Thermo Fisher Scientific) was added to the culture medium 5 min before cells being washed with PBS and immunostained as described above. Images of the monolayers were made in an unbiased manner, and the number of cells in interphase and mitosis (metaphase) that showed streptavidin accumulation below their cell–cell contacts was quantified. Mitotic cells that also had mitotic neighbors were excluded from the analyses.

Cellular confinement

MDCK cells expressing GFP-vinculin and H2B-mCherry were cultured in Collagen I–coated glass-bottom dishes (WillCo-dish)

and confined in a defined height of 6 µm as previously described (Le Berre et al., 2012). Briefly, micropillar spacers of 6-µm height were molded onto a thin layer of polydimethylsiloxane (PDMS) coating 10-mm-diameter glass coverslips. A precision vacuum controller (VG1006; Elveflow) operating a custom-made suction cup device gently positioned the textured slide onto the cells. Cells were incubated with 10 µM RO-3306 (Enzolifesci) 30 min before confinement to prevent them from entering mitosis, and RO-3306 was washed out directly before image acquisition. Imaging was performed on a Zeiss AxioObserver Z1 microscope equipped with a Yokogawa CSU-W1 spinning disc and Photometrics Prime 95B camera using a 63× oil objective (NA = 1.4), with a 3–5-min time interval (Fig. 3, C and D) at 37 C° and 5% CO_2 in a temperature- and CO_2-controlled incubator. In cells that were successfully confined (<1.2× decrease in cell perimeter upon mitotic entry, for which 6/24 cells were excluded) the distribution of GFP-vinculin was analyzed from whole z-stacks (Fig. 3, E and F). Cells that did not complete mitosis were excluded from the quantification, as well as cells that were already in mitosis before confinement.

Statistical analyses

All statistical analyses were performed using Prism 8 software (GraphPad). Each condition was tested for normality using a D'Agostino and Pearson test, and only when all conditions passed the normality test, a parametric test was performed. The statistical tests that were used (paired *t* tests, unpaired *t* tests, Wilcoxon matched-pairs signed-rank tests, and Mann–Whitney tests) are indicated in the figure legends. All statistical tests were two-sided.

Code availability

The Python scripts used in this manuscript (V1) for the analyses of junctional strain are available at https://github.com/Gloerichlab/Junction_strain_Monster-et-al-2021.

Online supplemental material

Fig. S1 accompanies Fig. 1 and shows additional morphological and nanoscissor ablation analyses of mitotic cell–cell junctions. Fig. S2 accompanies Fig. 2 and shows control experiments for the recruitment of vinculin to E-cadherin adhesions in mitotic cells and the dependence on E-cadherin–mediated force transmission. Fig. S3 accompanies Fig. 3 and shows accumulation of myosin at the mitotic cell cortex. Fig. S4 accompanies Fig. 4 and shows characterization of α-catenin$^{\Delta VBS}$ cells and loss of barrier integrity in vinculin knockdown cells. Fig. S5 accompanies Figs. 5 and 6 and shows control experiments for the asymmetric recruitment of vinculin to mitotic cell–cell adhesions and characterization of α-catenin^{CA} cells. Videos show cell division within a monolayer of MDCK cells expressing GFP–α-catenin (Video 1), GFP-vinculin (Video 3), GFP-vinculin in the absence of endogenous vinculin (Video 4), unconjugated GFP (Video 5), GFP–myosin IIA (Video 7), GFP-vinculin in the presence of blebbistatin (Video 8), or GFP-vinculin during and upon release of confinement (Video 9). Video 2 shows laser ablation and subsequent recoil of a junction neighboring a mitotic cell. Video 6 shows the gradual reduction of GFP-vinculin at mitotic junctions following release of tension by laser ablation. Video 10 accompanies Fig. 5 A and shows a z-stack of a mitotic cell expressing mScarlet-vinculin with a neighbor expressing GFP-vinculin.

Acknowledgments

We thank the imaging facility at the Princess Máxima Center for Pediatric Oncology (Utrecht, The Netherlands) for assistance with two-photon microscopy experiments. We thank Gerard van der Krogt (University Medical Center Utrecht) for generating α-catenin$^{\Delta VBS}$ cells, Brenton Hoffmann (Duke University, Durham, NC) for the vinculin rescue cell line, and members of our laboratories for helpful discussions and critical reading of the manuscript.

This work was supported by the Netherlands Organization for Scientific Research (NWO; 016.Vidi.189.166 and NWO gravitational program CancerGenomiCs.nl, awarded to M. Gloerich) and the European Commission (H2020-FETPROACT-01-2016-731957, awarded to J. de Rooij).

The authors declare no competing financial interests.

Author contributions: J.L. Monster, L. Donker, and M. Gloerich conceived the study. J.L. Monster, L. Donker, M.J. Vliem, and M. Gloerich performed experiments and analyzed data. Z. Win, H.K. Matthews, and B. Baum aided in the confinement experiments. J. Cheah and S. Yamada provided reagents. J. de Rooij provided reagents and feedback throughout the study. J.L. Monster, L. Donker, and M. Gloerich wrote the manuscript with input from all authors. M. Gloerich supervised the study.

Submitted: 28 January 2020
Revised: 23 December 2020
Accepted: 11 February 2021

References

Adriaans, I.E., A. Basant, B. Ponsioen, M. Glotzer, and S.M.A. Lens. 2019. PLK1 plays dual roles in centralspindlin regulation during cytokinesis. *J. Cell Biol.* 218:1250–1264. https://doi.org/10.1083/jcb.201805036

Alatortsev, V.E., I.A. Kramerova, M.V. Frolov, S.A. Lavrov, and E.D. Westphal. 1997. Vinculin gene is non-essential in Drosophila melanogaster. *FEBS Lett.* 413:197–201. https://doi.org/10.1016/S0014-5793(97)00901-0

Bachir, A.I., A.R. Horwitz, W.J. Nelson, and J.M. Bianchini. 2017. Actin-Based Adhesion Modules Mediate Cell Interactions with the Extracellular Matrix and Neighboring Cells. *Cold Spring Harb. Perspect. Biol.* 9: a023234. https://doi.org/10.1101/cshperspect.a023234

Baker, J., and D. Garrod. 1993. Epithelial cells retain junctions during mitosis. *J. Cell Sci.* 104:415–425.

Bauer, A., H. Lickert, R. Kemler, and J. Stappert. 1998. Modification of the E-cadherin-catenin complex in mitotic Madin-Darby canine kidney epithelial cells. *J. Biol. Chem.* 273:28314–28321. https://doi.org/10.1074/jbc.273.43.28314

Bindels, D.S., L. Haarbosch, L. van Weeren, M. Postma, K.E. Wiese, M. Mastop, S. Aumonier, G. Gotthard, A. Royant, M.A. Hink, and T.W.J. Gadella Jr. 2017. mScarlet: a bright monomeric red fluorescent protein for cellular imaging. *Nat. Methods.* 14:53–56. https://doi.org/10.1038/nmeth.4074

Blanpain, C., V. Horsley, and E. Fuchs. 2007. Epithelial stem cells: turning over new leaves. *Cell.* 128:445–458. https://doi.org/10.1016/j.cell.2007.01.014

Buckley, C.D., J. Tan, K.L. Anderson, D. Hanein, N. Volkmann, W.I. Weis, W.J. Nelson, and A.R. Dunn. 2014. Cell adhesion. The minimal cadherin-catenin complex binds to actin filaments under force. *Science.* 346: 1254211. https://doi.org/10.1126/science.1254211

Carreno, S., I. Kouranti, E.S. Glusman, M.T. Fuller, A. Echard, and F. Payre. 2008. Moesin and its activating kinase Slik are required for cortical stability and microtubule organization in mitotic cells. *J. Cell Biol.* 180: 739–746. https://doi.org/10.1083/jcb.200709161

Champion, L., M.I. Linder, and U. Kutay. 2017. Cellular Reorganization during Mitotic Entry. *Trends Cell Biol.* 27:26–41. https://doi.org/10.1016/j.tcb.2016.07.004

Chan, C.J., M. Costanzo, T. Ruiz-Herrero, G. Mönke, R.J. Petrie, M. Bergert, A. Diz-Muñoz, L. Mahadevan, and T. Hiiragi. 2019. Hydraulic control of mammalian embryo size and cell fate. *Nature.* 571:112–116. https://doi.org/10.1038/s41586-019-1309-x

Charras, G., and A.S. Yap. 2018. Tensile Forces and Mechanotransduction at Cell-Cell Junctions. *Curr. Biol.* 28:R445–R457. https://doi.org/10.1016/j.cub.2018.02.003

Chen, T., T.B. Saw, R.-M. Mège, and B. Ladoux. 2018. Mechanical forces in cell monolayers. *Journal of Cell Science.* 131:jcs218156. https://doi.org/10.1242/jcs.218156.

Cramer, L.P., and T.J. Mitchison. 1997. Investigation of the mechanism of retraction of the cell margin and rearward flow of nodules during mitotic cell rounding. *Mol. Biol. Cell.* 8:109–119. https://doi.org/10.1091/mbc.8.1.109

Dao, V.T., A.G. Dupuy, O. Gavet, E. Caron, and J. de Gunzburg. 2009. Dynamic changes in Rap1 activity are required for cell retraction and spreading during mitosis. *J. Cell Sci.* 122:2996–3004. https://doi.org/10.1242/jcs.041301

Daub, H., J.V. Olsen, M. Bairlein, F. Gnad, F.S. Oppermann, R. Körner, Z. Greff, G. Kéri, O. Stemmann, and M. Mann. 2008. Kinase-selective enrichment enables quantitative phosphoproteomics of the kinome across the cell cycle. *Mol. Cell.* 31:438–448. https://doi.org/10.1016/j.molcel.2008.07.007

Dorland, Y.L., T.S. Malinova, A.-M.D. van Stalborch, A.G. Grieve, D. van Geemen, N.S. Jansen, B.-J. de Kreuk, K. Nawaz, J. Kole, D. Geerts, et al. 2016. The F-BAR protein pacsin2 inhibits asymmetric VE-cadherin internalization from tensile adherens junctions. *Nat. Commun.* 7:12210. https://doi.org/10.1038/ncomms12210

Drost, J., R.H. van Jaarsveld, B. Ponsioen, C. Zimberlin, R. van Boxtel, A. Buijs, N. Sachs, R.M. Overmeer, G.J. Offerhaus, H. Begthel, et al. 2015. Sequential cancer mutations in cultured human intestinal stem cells. *Nature.* 521:43–47. https://doi.org/10.1038/nature14415

Guillot, C., and T. Lecuit. 2013. Adhesion disengagement uncouples intrinsic and extrinsic forces to drive cytokinesis in epithelial tissues. *Dev. Cell.* 24:227–241. https://doi.org/10.1016/j.devcel.2013.01.010

Hayer, A., L. Shao, M. Chung, L.-M. Joubert, H.W. Yang, F.-C. Tsai, A. Bisaria, E. Betzig, and T. Meyer. 2016. Engulfed cadherin fingers are polarized junctional structures between collectively migrating endothelial cells. *Nat. Cell Biol.* 18:1311–1323. https://doi.org/10.1038/ncb3438

Herbomel, G., G. Hatte, J. Roul, S. Padilla-Parra, J.P. Tassan, and M. Tramier. 2017. Actomyosin-generated tension on cadherin is similar between dividing and non-dividing epithelial cells in early Xenopus laevis embryos. *Sci. Rep.* 7:45058. https://doi.org/10.1038/srep45058

Higashi, T., T.R. Arnold, R.E. Stephenson, K.M. Dinshaw, and A.L. Miller. 2016. Maintenance of the Epithelial Barrier and Remodeling of Cell-Cell Junctions during Cytokinesis. *Curr. Biol.* 26:1829–1842. https://doi.org/10.1016/j.cub.2016.05.036

Huveneers, S., J. Oldenburg, E. Spanjaard, G. van der Krogt, I. Grigoriev, A. Akhmanova, H. Rehmann, and J. de Rooij. 2012. Vinculin associates with endothelial VE-cadherin junctions to control force-dependent remodeling. *J. Cell Biol.* 196:641–652. https://doi.org/10.1083/jcb.201108120

Ibar, C., E. Kirichenko, B. Keepers, E. Enners, K. Fleisch, and K.D. Irvine. 2018. Tension-dependent regulation of mammalian Hippo signaling through LIMD1. *J. Cell Sci.* 131:jcs214700. https://doi.org/10.1242/jcs.214700

Ishiyama, N., R. Sarpal, M.N. Wood, S.K. Barrick, T. Nishikawa, H. Hayashi, A.B. Kobb, A.S. Flozak, A. Yemelyanov, R. Fernandez-Gonzalez, et al. 2018. Force-dependent allostery of the α-catenin actin-binding domain controls adherens junction dynamics and functions. *Nat. Commun.* 9: 5121. https://doi.org/10.1038/s41467-018-07481-7

Ito, S., S. Okuda, M. Abe, M. Fujimoto, T. Onuki, T. Nishimura, and M. Takeichi. 2017. Induced cortical tension restores functional junctions in adhesion-defective carcinoma cells. *Nat. Commun.* 8:1834. https://doi.org/10.1038/s41467-017-01945-y

Jorrisch, M.H., W. Shih, and S. Yamada. 2013. Myosin IIA deficient cells migrate efficiently despite reduced traction forces at cell periphery. *Biol. Open.* 2:368–372. https://doi.org/10.1242/bio.20133707

Kunda, P., A.E. Pelling, T. Liu, and B. Baum. 2008. Moesin controls cortical rigidity, cell rounding, and spindle morphogenesis during mitosis. *Curr. Biol.* 18:91–101. https://doi.org/10.1016/j.cub.2007.12.051

Ladoux, B., E. Anon, M. Lambert, A. Rabodzey, P. Hersen, A. Buguin, P. Silberzan, and R.-M. Mège. 2010. Strength dependence of cadherin-mediated adhesions. *Biophys. J.* 98:534–542. https://doi.org/10.1016/j.bpj.2009.10.044

Lancaster, O.M., and B. Baum. 2014. Shaping up to divide: coordinating actin and microtubule cytoskeletal remodelling during mitosis. *Semin. Cell Dev. Biol.* 34:109–115. https://doi.org/10.1016/j.semcdb.2014.02.015

Lancaster, O.M., M. Le Berre, A. Dimitracopoulos, D. Bonazzi, E. Zlotek-Zlotkiewicz, R. Picone, T. Duke, M. Piel, and B. Baum. 2013. Mitotic rounding alters cell geometry to ensure efficient bipolar spindle formation. *Dev. Cell.* 25:270–283. https://doi.org/10.1016/j.devcel.2013.03.014

Le Berre, M., J. Aubertin, and M. Piel. 2012. Fine control of nuclear confinement identifies a threshold deformation leading to lamina rupture and induction of specific genes. *Integr. Biol.* 4:1406–1414. https://doi.org/10.1039/c2ib20056b

le Duc, Q., Q. Shi, I. Blonk, A. Sonnenberg, N. Wang, D. Leckband, and J. de Rooij. 2010. Vinculin potentiates E-cadherin mechanosensing and is recruited to actin-anchored sites within adherens junctions in a myosin II-dependent manner. *J. Cell Biol.* 189:1107–1115. https://doi.org/10.1083/jcb.201001149

Leckband, D.E., and J. de Rooij. 2014. Cadherin adhesion and mechanotransduction. *Annu. Rev. Cell Dev. Biol.* 30:291–315. https://doi.org/10.1146/annurev-cellbio-100913-013212

Leckband, D.E., Q. le Duc, N. Wang, and J. de Rooij. 2011. Mechanotransduction at cadherin-mediated adhesions. *Curr. Opin. Cell Biol.* 23: 523–530. https://doi.org/10.1016/j.ceb.2011.08.003

Lecuit, T., and A.S. Yap. 2015. E-cadherin junctions as active mechanical integrators in tissue dynamics. *Nat. Cell Biol.* 17:533–539. https://doi.org/10.1038/ncb3136

Leerberg, J.M., G.A. Gomez, S. Verma, E.J. Moussa, S.K. Wu, R. Priya, B.D. Hoffman, C. Grashoff, M.A. Schwartz, and A.S. Yap. 2014. Tension-sensitive actin assembly supports contractility at the epithelial zonula adherens. *Curr. Biol.* 24:1689–1699. https://doi.org/10.1016/j.cub.2014.06.028

Liang, X., M. Michael, and G.A. Gomez. 2016. Measurement of Mechanical Tension at Cell-cell Junctions Using Two-photon Laser Ablation. *Bio Protoc.* 6:e2068. https://doi.org/10.21769/BioProtoc.2068

Liu, Z., J.L. Tan, D.M. Cohen, M.T. Yang, N.J. Sniadecki, S.A. Ruiz, C.M. Nelson, and C.S. Chen. 2010. Mechanical tugging force regulates the size of cell-cell junctions. *Proc. Natl. Acad. Sci. USA.* 107:9944–9949. https://doi.org/10.1073/pnas.0914547107

Maddox, A.S., and K. Burridge. 2003. RhoA is required for cortical retraction and rigidity during mitotic cell rounding. *J. Cell Biol.* 160:255–265. https://doi.org/10.1083/jcb.200207130

Maki, K., S.-W. Han, Y. Hirano, S. Yonemura, T. Hakoshima, and T. Adachi. 2016. Mechano-adaptive sensory mechanism of α-catenin under tension. *Sci. Rep.* 6:24878. https://doi.org/10.1038/srep24878

Manning, L.A., K.Z. Perez-Vale, K.N. Schaefer, M.T. Sewell, and M. Peifer. 2019. The *Drosophila* Afadin and ZO-1 homologues Canoe and Polychaetoid act in parallel to maintain epithelial integrity when challenged by adherens junction remodeling. *Mol. Biol. Cell.* 30:1938–1960. https://doi.org/10.1091/mbc.E19-04-0209

Marchesi, S., F. Montani, G. Deflorian, R. D'Antuono, A. Cuomo, S. Bologna, C. Mazzoccoli, T. Bonaldi, P.P. Di Fiore, and F. Nicassio. 2014. DEPDC1B coordinates de-adhesion events and cell-cycle progression at mitosis. *Dev. Cell.* 31:420–433. https://doi.org/10.1016/j.devcel.2014.09.009

Mashburn, D.N., H.E. Lynch, X. Ma, and M.S. Hutson. 2012. Enabling user-guided segmentation and tracking of surface-labeled cells in time-lapse image sets of living tissues. *Cytometry A.* 81:409–418. https://doi.org/10.1002/cyto.a.22034

Matsuzawa, K., T. Himoto, Y. Mochizuki, and J. Ikenouchi. 2018. α-Catenin Controls the Anisotropy of Force Distribution at Cell-Cell Junctions during Collective Cell Migration. *Cell Rep.* 23:3447–3456. https://doi.org/10.1016/j.celrep.2018.05.070

Matthews, H.K., U. Delabre, J.L. Rohn, J. Guck, P. Kunda, and B. Baum. 2012. Changes in Ect2 localization couple actomyosin-dependent cell shape changes to mitotic progression. *Dev. Cell.* 23:371–383. https://doi.org/10.1016/j.devcel.2012.06.003

Mège, R.M., and N. Ishiyama. 2017. Integration of Cadherin Adhesion and Cytoskeleton at *Adherens* Junctions. *Cold Spring Harb. Perspect. Biol.* 9: a028738. https://doi.org/10.1101/cshperspect.a028738

Oldenburg, J., G. van der Krogt, F. Twiss, A. Bongaarts, Y. Habani, J.A. Slotman, A. Houtsmuller, S. Huveneers, and J. de Rooij. 2015. VASP, zyxin and TES are tension-dependent members of Focal Adherens Junctions independent of the α-catenin-vinculin module. *Sci. Rep.* 5:17225. https://doi.org/10.1038/srep17225

Olsen, J.V., M. Vermeulen, A. Santamaria, C. Kumar, M.L. Miller, L.J. Jensen, F. Gnad, J. Cox, T.S. Jensen, E.A. Nigg, et al. 2010. Quantitative phosphoproteomics reveals widespread full phosphorylation site occupancy during mitosis. *Sci. Signal.* 3:ra3. https://doi.org/10.1126/scisignal.2000475

Ortega, F.E., M. Rengarajan, N. Chavez, P. Radhakrishnan, M. Gloerich, J. Bianchini, K. Siemers, W.S. Luckett, P. Lauer, W.J. Nelson, and J.A. Theriot. 2017. Adhesion to the host cell surface is sufficient to mediate *Listeria monocytogenes* entry into epithelial cells. *Mol. Biol. Cell.* 28: 2945–2957. https://doi.org/10.1091/mbc.e16-12-0851

Pannekoek, W.-J., J. de Rooij, and M. Gloerich. 2019. Force transduction by cadherin adhesions in morphogenesis. *F1000Res.* 8. doi:. https://doi.org/10.12688/f1000research.18779.1

Petridou, N.I., S. Grigolon, G. Salbreux, E. Hannezo, and C.-P.P. Heisenberg. 2019. Fluidization-mediated tissue spreading by mitotic cell rounding and non-canonical Wnt signalling. *Nat. Cell Biol.* 21:169–178. https://doi.org/10.1038/s41556-018-0247-4

Ramanathan, S.P., J. Helenius, M.P. Stewart, C.J. Cattin, A.A. Hyman, and D.J. Muller. 2015. Cdk1-dependent mitotic enrichment of cortical myosin II promotes cell rounding against confinement. *Nat. Cell Biol.* 17:148–159. https://doi.org/10.1038/ncb3098

Reinsch, S., and E. Karsenti. 1994. Orientation of spindle axis and distribution of plasma membrane proteins during cell division in polarized MDCKII cells. *J. Cell Biol.* 126:1509–1526. https://doi.org/10.1083/jcb.126.6.1509

Rosa, A., E. Vlassaks, F. Pichaud, and B. Baum. 2015. Ect2/Pbl acts via Rho and polarity proteins to direct the assembly of an isotropic actomyosin cortex upon mitotic entry. *Dev. Cell.* 32:604–616. https://doi.org/10.1016/j.devcel.2015.01.012

Sato, T., R.G. Vries, H.J. Snippert, M. van de Wetering, N. Barker, D.E. Stange, J.H. van Es, A. Abo, P. Kujala, P.J. Peters, and H. Clevers. 2009. Single Lgr5 stem cells build crypt-villus structures in vitro without a mesenchymal niche. *Nature.* 459:262–265. https://doi.org/10.1038/nature07935

Sawyer, J.K., N.J. Harris, K.C. Slep, U. Gaul, and M. Peifer. 2009. The Drosophila afadin homologue Canoe regulates linkage of the actin cytoskeleton to adherens junctions during apical constriction. *J. Cell Biol.* 186:57–73. https://doi.org/10.1083/jcb.200904001

Sorce, B., C. Escobedo, Y. Toyoda, M.P. Stewart, C.J. Cattin, R. Newton, I. Banerjee, A. Stettler, B. Roska, S. Eaton, et al. 2015. Mitotic cells contract actomyosin cortex and generate pressure to round against or escape epithelial confinement. *Nat. Commun.* 6:8872. https://doi.org/10.1038/ncomms9872

Stewart, M.P., J. Helenius, Y. Toyoda, S.P. Ramanathan, D.J. Muller, and A.A. Hyman. 2011. Hydrostatic pressure and the actomyosin cortex drive mitotic cell rounding. *Nature.* 469:226–230. https://doi.org/10.1038/nature09642

Sumida, G.M., T.M. Tomita, W. Shih, and S. Yamada. 2011. Myosin II activity dependent and independent vinculin recruitment to the sites of E-cadherin-mediated cell-cell adhesion. *BMC Cell Biol.* 12:48. https://doi.org/10.1186/1471-2121-12-48

Takeichi, M. 2014. Dynamic contacts: rearranging adherens junctions to drive epithelial remodelling. *Nat. Rev. Mol. Cell Biol.* 15:397–410. https://doi.org/10.1038/nrm3802

Taubenberger, A.V., B. Baum, and H.K. Matthews. 2020. The Mechanics of Mitotic Cell Rounding. *Front. Cell Dev. Biol.* 8:687. https://doi.org/10.3389/fcell.2020.00687

Teo, J.L., V.M. Tomatis, L. Coburn, A.K. Lagendijk, I.-M. Schouwenaar, S. Budnar, T.E. Hall, S. Verma, R.W. McLachlan, B.M. Hogan, et al. 2020. Src kinases relax adherens junctions between the neighbors of apoptotic cells to permit apical extrusion. *Mol. Biol. Cell.* 31:2557–2569. https://doi.org/10.1091/mbc.E20-01-0084

Thomas, R., R. Apps, Y. Qi, X. Gao, V. Male, C. O'hUigin, G. O'Connor, D. Ge, J. Fellay, J.N. Martin, et al. 2009. HLA-C cell surface expression and control of HIV/AIDS correlate with a variant upstream of HLA-C. *Nat. Genet.* 41:1290–1294. https://doi.org/10.1038/ng.486

Thomas, W.A., C. Boscher, Y.S. Chu, D. Cuvelier, C. Martinez-Rico, R. Seddiki, J. Heysch, B. Ladoux, J.P. Thiery, R.M. Mege, and S. Dufour. 2013. α-Catenin and vinculin cooperate to promote high E-cadherin-based adhesion strength. *J. Biol. Chem.* 288:4957–4969. https://doi.org/10.1074/jbc.M112.403774

Troxell, M.L., S. Gopalakrishnan, J. McCormack, B.A. Poteat, J. Pennington, S.M. Garringer, E.E. Schneeberger, W.J. Nelson, and J.A. Marrs. 2000. Inhibiting cadherin function by dominant mutant E-cadherin expression increases the extent of tight junction assembly. *J. Cell Sci.* 113: 985–996.

Twiss, F., Q. Le Duc, S. Van Der Horst, H. Tabdili, G. Van Der Krogt, N. Wang, H. Rehmann, S. Huveneers, D.E. Leckband, and J. De Rooij. 2012. Vinculin-dependent Cadherin mechanosensing regulates efficient epithelial barrier formation. *Biol. Open.* 1:1128–1140. https://doi.org/10.1242/bio.20122428

van der Wal, J., R. Habets, P. Várnai, T. Balla, and K. Jalink. 2001. Monitoring agonist-induced phospholipase C activation in live cells by fluorescence resonance energy transfer. *J. Biol. Chem.* 276:15337–15344. https://doi.org/10.1074/jbc.M007194200

Yamada, S., S. Pokutta, F. Drees, W.I. Weis, and W.J. Nelson. 2005. Deconstructing the cadherin-catenin-actin complex. *Cell.* 123:889–901. https://doi.org/10.1016/j.cell.2005.09.020

Yamakita, Y., G. Totsukawa, S. Yamashiro, D. Fry, X. Zhang, S.K. Hanks, and F. Matsumura. 1999. Dissociation of FAK/p130(CAS)/c-Src complex during mitosis: role of mitosis-specific serine phosphorylation of FAK. *J. Cell Biol.* 144:315–324. https://doi.org/10.1083/jcb.144.2.315

Yao, M., W. Qiu, R. Liu, A.K. Efremov, P. Cong, R. Seddiki, M. Payre, C.T. Lim, B. Ladoux, R.-M. Mège, and J. Yan. 2014. Force-dependent conformational switch of α-catenin controls vinculin binding. *Nat. Commun.* 5: 4525. https://doi.org/10.1038/ncomms5525

Yonemura, S., Y. Wada, T. Watanabe, A. Nagafuchi, and M. Shibata. 2010. alpha-Catenin as a tension transducer that induces adherens junction development. *Nat. Cell Biol.* 12:533–542. https://doi.org/10.1038/ncb2055

Supplemental material

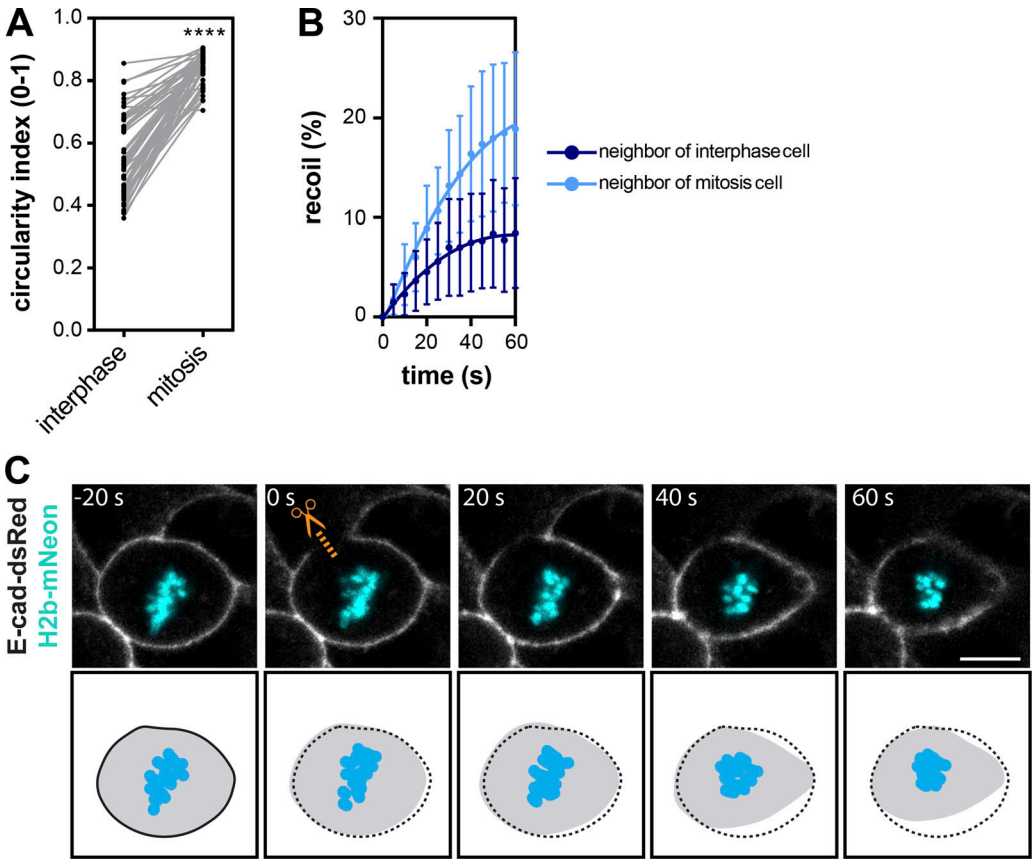

Figure S1. **Morphological and nanoscissor laser ablation analyses of mitotic cells. (A)** Quantification of the circularity ($4\pi \times \text{area/perimeter}^2$) of MDCK cells in interphase and following entry into mitosis ($n = 55$). Quantified data were pooled from three independent experiments. ****, $P < 0.0001$; Wilcoxon matched-pairs signed-rank test. **(B)** Quantification of relative recoil of cell–cell contacts neighboring interphase (dark blue; $n = 24$) or mitotic (blue; $n = 22$) cells after laser cutting, defined as the relative increase in distance between vertices (length/initial length). Dots represent the mean recoil distance with SD, with lines showing the best-fit single exponential curve. Data were pooled from two independent experiments. **(C)** Top: Representative still images of a mitotic MDCK cell expressing E-cadherin–DsRed and H2B-mNeongreen after laser ablation of the mitotic cortex (illustrated by orange scissors). Bottom: Visualization of the changes in cell shape (gray) compared with the preablated mitotic cell (black dotted line). Scale bar, 10 µm. E-cad, E-cadherin.

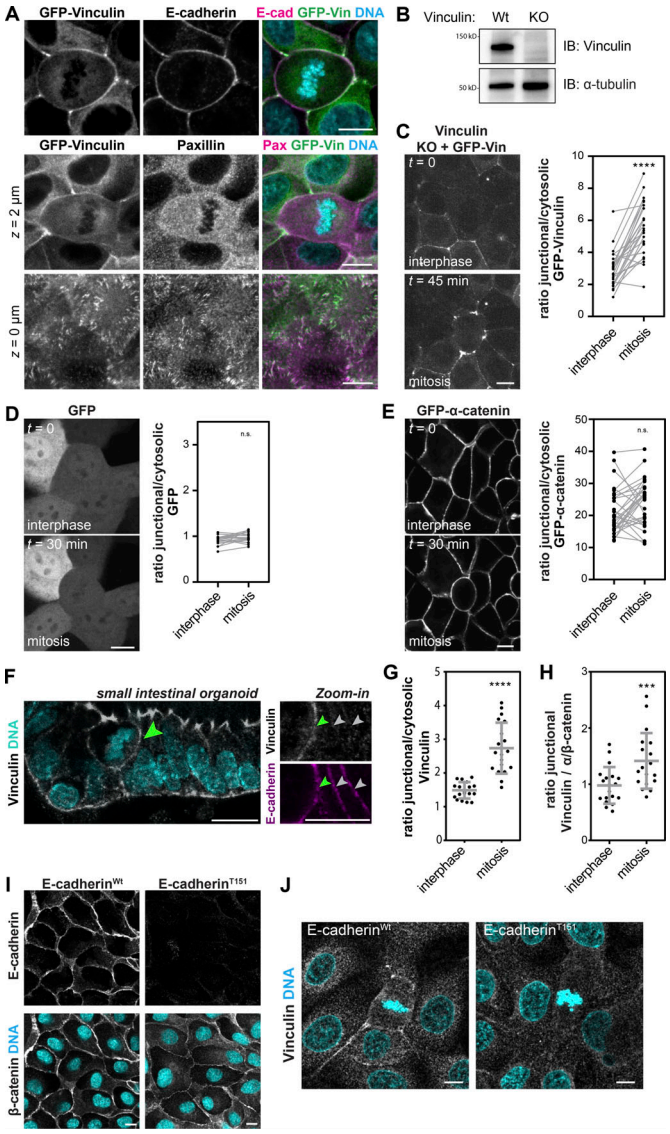

Figure S2. **Vinculin is enriched at cadherin-based adhesions of mitotic cells in MDCK monolayers and intestinal organoids, dependent on E-cadherin force transmission. (A)** Immunostaining of MDCK cells expressing GFP-vinculin for endogenous E-cadherin and paxillin, together with DAPI. While GFP-vinculin is able to localize to both adherens junctions (E-cadherin) and focal adhesions (paxillin), the observed mitotic enrichment is specific to adherens junctions. **(B)** WB of lysates from parental and vinculin knockout (KO) MDCK cells probed for vinculin and α-tubulin. **(C)** Representative image (z-projection) of MDCK vinculin KO cells expressing GFP-vinculin (Video 4), and quantification of the ratio of junctional versus cytosolic GFP-vinculin in interphase and following entry in mitosis (n = 26). ****, P < 0.0001; Wilcoxon matched-pairs signed-rank test. **(D)** Representative image (z-projection) of MDCK cells expressing GFP (Video 5), and quantification of the ratio of junctional versus cytosolic GFP in interphase and following entry in mitosis (n = 18). Data were pooled from three independent experiments. n.s., not significant (P = 0.09); Wilcoxon matched-pairs signed-rank test. **(E)** Representative image (z-projection) of MDCK cells expressing GFP–α-catenin (Video 1), and quantification of the ratio of junctional versus cytosolic GFP–α-catenin in interphase and following entry in mitosis (n = 30). Data were pooled from three independent experiments. n.s., not significant (P = 0.07); Wilcoxon matched-pairs signed-rank test. **(F)** Representative example of immunostaining for endogenous vinculin and E-cadherin in murine small intestinal organoids, together with DAPI. The green arrowhead indicates the cell–cell junction of a mitotic cell; gray arrowheads indicate cell–cell junctions of neighboring cells in interphase. Note that while vinculin accumulates at the lateral junction of mitotic cells, it is present at the apical junction of both mitotic and interphase cells, as well as in integrin adhesions in interphase cells. Scale bars, 10 µm. **(G)** Quantification of the ratio of junctional versus cytosolic vinculin in mitotic and interphase cells in murine small intestinal organoids (n = 19). Gray bars show the mean ratio with SD. Data were pooled from two independent experiments. ****, P < 0.0001; paired t test. **(H)** Quantification of the ratio of the intensity of junctional vinculin relative to the intensity of a junctional marker (α-catenin or β-catenin) in mitotic and interphase cells in murine small intestinal organoids (n = 19). Gray bars show the mean ratio with SD. Data were pooled from two independent experiments. ***, P = 0.0002; paired t test. **(I)** Immunostaining of MDCK cells, with and without induction of E-cadherin^{T151} expression, for endogenous E-cadherin and β-catenin, together with DAPI. E-cadherin^{T151} contains a truncated extracellular domain and can therefore not transmit forces between cells, but maintains an intact cytosolic tail that binds catenin proteins and the actin cytoskeleton (Troxell et al., 2000). The expression of E-cadherin^{T151} leads to the down-regulation of endogenous cadherins, but cells retain their monolayer due to the presence of other cell–cell adhesions (Troxell et al., 2000). Note that the antibody for E-cadherin recognizes the extracellular domain of E-cadherin, and therefore does not visualize E-cadherin^{T151}. **(J)** Representative image (z-projection) of immunostaining of MDCK cells induced for E-cadherin^{T151} expression or uninduced (E-cadherin^{WT}) for endogenous vinculin, together with DAPI. All scale bars, 10 µm. E-cad, E-cadherin; IB, immunoblot; Pax, paxillin; Vin, vinculin.

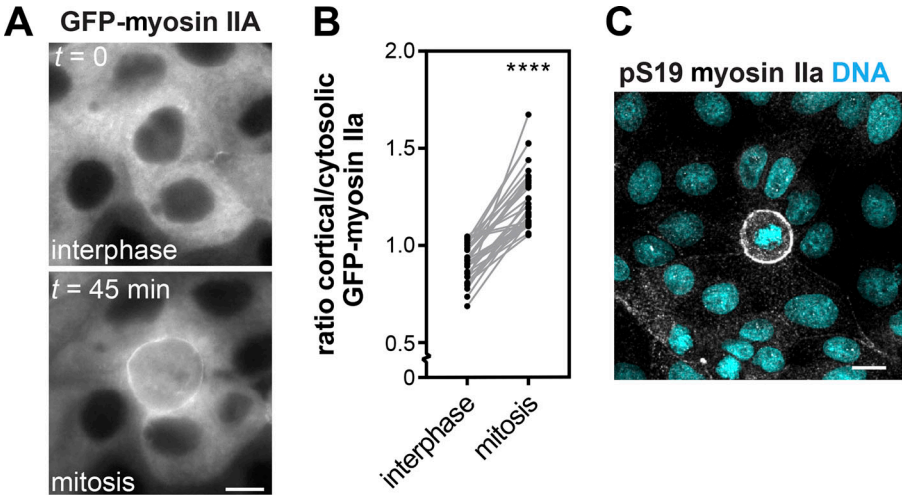

Figure S3. **Mitotic rounding of epithelial cells is accompanied by an increase in cortical myosin. (A)** Representative image of MDCK cells expressing GFP–myosin IIA in interphase and following entry in mitosis (Video 7). **(B)** Quantification of the ratio of cortical versus cytosolic GFP–myosin IIA in MDCK cells in interphase and following entry in mitosis (n = 30). Data were pooled from three independent experiments. ****, $P < 0.0001$; paired t test. **(C)** Representative image (z-projection) of immunostaining of MDCK cells for phospho-S19 myosin IIA, together with DAPI, showing an increase in myosin IIA phosphorylation upon mitotic entry. All scale bars, 10 µm. t, time.

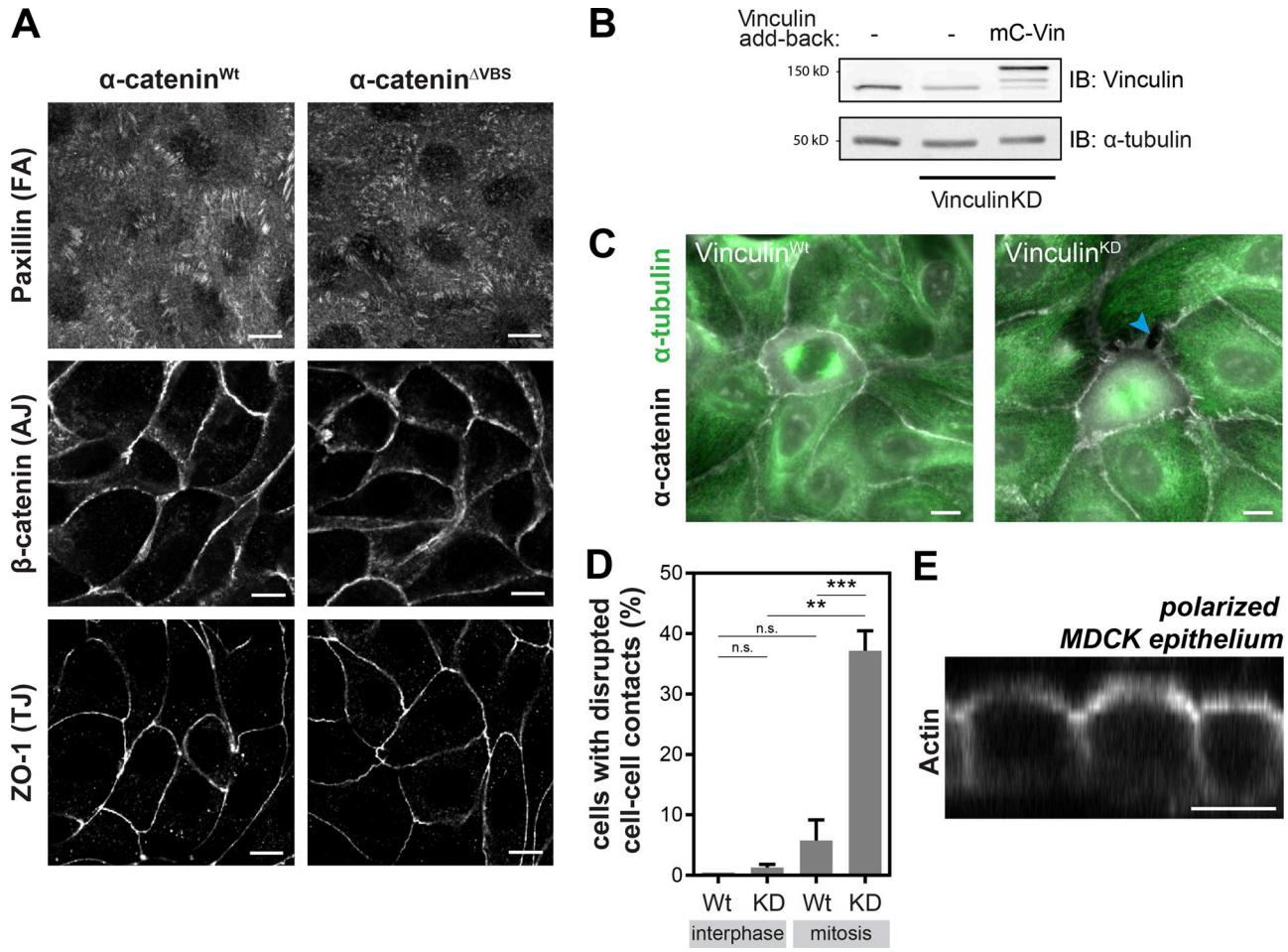

Figure S4. **Validation of the vinculin-dependent junctional reinforcement of mitotic cell–cell junctions. (A)** Immunostaining of MDCK cells expressing WT- or ΔVBS α-catenin for endogenous paxillin, β-catenin, and ZO-1, showing that focal adhesions (FA) are maintained in α-catenin$^{\Delta VBS}$ cells, and no apparent differences in adherens junctions (AJ) and tight junctions (TJ)) in α-catenin$^{\Delta VBS}$ cells compared with WT cells during interphase. **(B)** WB of lysates from parental-, vinculin knockdown (KD)-, and vinculin KD with addback of mCherry-vinculin MDCK cells probed for vinculin and α-tubulin. **(C)** Immunostainings of MDCK cells with vinculin knockdown (KD), and vinculin KD with addback of mCherry-vinculin, for α-catenin and α-tubulin to visualize mitotic cells and the integrity of cell–cell contacts. Blue arrowhead indicates a disrupted cell–cell contact. **(D)** Quantification of the fraction of mitotic and interphase cells in which cell–cell contacts are perturbed, in MDCK monolayers with vinculin KD, and vinculin KD with addback of mCherry-vinculin. Data were pooled from three independent experiments, with at least 25 cells analyzed per condition in each experiment. Gray bars represent the mean and SD of the average fraction of disrupted cell–cell contacts in the independent experiments. **, P = 0.0021; ***, P = 0.0008; n.s., not significant (P = 0.12, P = 0.10 respectively); paired *t* test. **(E)** Representative x,z-projection of a polarized MDCK monolayer cultured under conditions used for the permeability assay (Fig. 4, C and D), in which apicobasal polarization is indicated by the apical actin brush border that is visualized with SiR-Actin. Scale bars, 10 µm. IB, immunoblot; mC, mCherry; Vin, vinculin.

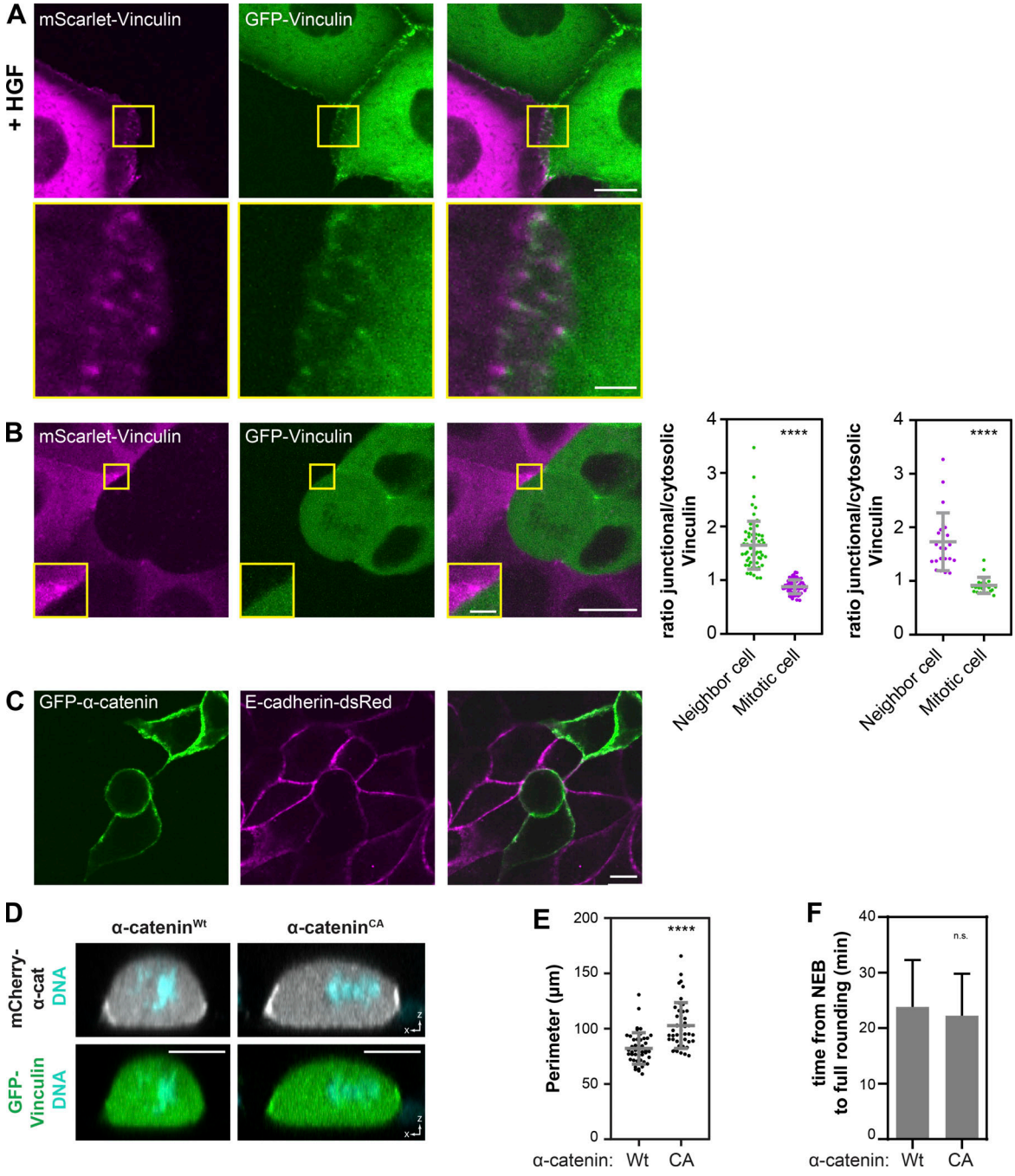

Figure S5. **Asymmetric composition of mitotic cell–cell junctions due to selective ability of α-catenin in neighbors of mitotic cells to recruit vinculin.** **(A)** Coculture of MDCK cells expressing either GFP-vinculin or mScarlet-vinculin after 1 h incubation with 15 ng/ml HGF. A representative example (z-projection) with inset shows that vinculin is recruited to cell–cell adhesions upon HGF-induced cell scattering, in both of the two cells forming the focal adherens junction. **(B)** Left: Representative image (z-projection) with inset of a mitotic cell expressing GFP-vinculin with a neighbor expressing mScarlet-vinculin, displaying a similar asymmetry as demonstrated in Fig. 5 A. Right: Quantifications of the ratio of junctional versus cytosolic vinculin intensity of mitotic cells and their interphase neighbors (as in Fig. 5 B), separated by the vinculin tag in the mitotic and neighboring cells (GFP represented by green dots, mScarlet by magenta dots; $n = 64$ and $n = 23$ junctions, respectively). Gray bars show the mean ratio with SD. These data demonstrate that the asymmetry is not dependent on the fluorophore tagged to vinculin. Data were pooled from three independent experiments. ****, $P < 0.0001$; Wilcoxon matched-pairs signed-rank test. **(C)** Coculture of MDCK cells expressing either α-catenin–GFP or E-cadherin–DsRed, with representative image of a mitotic cell expressing α-catenin–GFP that shows α-catenin remains present at the mitotic cortex. **(D)** x,z-representation of cocultures of parental MDCK cells and cells inducibly expressing either mCherry–α-catenin^{WT} (left) or mCherry-α-catenin$^{M319G,\ R326E}$ (α-catenin^{CA}; right), together with GFP-vinculin. Nuclei are visualized with Hoechst. **(E)** Quantification of cell perimeter of MDCK cells in metaphase expressing either WT- or CA α-catenin ($n = 45$ per condition). Gray bars show the mean cell perimeter with SD. Quantified data were pooled from three independent experiments. ****, $P < 0.0001$; Mann–Whitney. **(F)** Quantification of time from nuclear envelope breakdown (NEB) to full rounding in MDCK cells inducibly expressing either WT- ($n = 81$) or CA α-catenin ($n = 93$). Gray bars show the mean cell perimeter with SD. Quantified data were pooled from three independent experiments. n.s., not significant ($P = 0.17$); Mann–Whitney. All scale bars, 10 µm or 2 µm (insets, A and B). α-cat, α-catenin.

Video 1. **Mitosis within monolayer of MDCK cells expressing GFP-α-catenin.** Time-lapse confocal imaging (z-projections) of monolayer of MDCK cells expressing GFP-α-catenin (grays). Time interval: 10 min (time: h:min:s; 6 fps). Scale bar: 10 µm. Accompanies Fig. S2 E.

Video 2. **Laser cutting of a junction neighboring a mitotic cell in MDCK cell monolayer.** Time-lapse confocal imaging of monolayer of MDCK cells expressing E-cadherin (E-cad)-dsRed (grays) and H2B-mNeongreen (neon, cyan). After 20 s, the actin cortex was cut using two-photon laser nanoscissors (orange scissors). Time interval: 4 s (time: h:min:s; 7 fps). Scale bar: 10 µm. Accompanies Fig. 1 F.

Video 3. **Mitosis within monolayer of MDCK cells expressing GFP-vinculin.** Time-lapse confocal imaging (z-projections) of monolayer of MDCK cells expressing GFP-Vinculin (grays). Time interval: 5 min (time: h:min:s; 10 fps). Scale bar: 10 µm. Accompanies Fig. 2 A.

Video 4. **Mitosis within monolayer of vinculin knockout (KO) MDCK cells expressing GFP-vinculin.** Time-lapse confocal imaging (z-projections) of monolayer of vinculin knockout (KO) MDCK cells expressing GFP-α-catenin (grays). Time interval: 15 min (time: h:min:s; 6 fps). Scale bar: 10 µm. Accompanies Fig. S2 C.

Video 5. **Mitosis within monolayer of MDCK cells expressing unconjugated GFP.** Time-lapse confocal imaging (z-projections) of monolayer of MDCK cells expressing unconjugated GFP (grays). Time interval: 10 min (time: h:min:s; 6 fps). Scale bar: 10 µm. Accompanies Fig. S2 D.

Video 6. **Loss of GFP-vinculin at mitotic junctions following release of tension by laser cutting of neighboring cell–cell junction.** Time-lapse confocal imaging of monolayer of MDCK cells expressing GFP-vinculin (grays). After 15 seconds, the actin cortex of a junction perpendicular to the mitotic cell was cut using two-photon laser nanoscissors (orange scissors) to relieve tension. Time interval: 5 s (time: h:min:s; 6 fps). Scale bar: 10 µm. Accompanies Fig. 2 H.

Video 7. **Mitosis within monolayer of MDCK cells expressing GFP-myosin IIA.** Time-lapse epifluoresence imaging of monolayer of MDCK cells expressing GFP-myosin IIa (grays). Time interval: 10 min (time: h:min:s; 7 fps). Scale bar: 10 µm. Accompanies Fig. S3 A.

Video 8. **Mitosis within monolayer of MDCK cells expressing GFP-vinculin in the presence of blebbistatin or DMSO.** Time-lapse confocal imaging (z-projections) of monolayer of MDCK cells expressing GFP-vinculin (grays). After 10 minutes, 10 µM para-nitro-blebbistatin (right, Blebbistatin) or DMSO (left, DMSO) was added for the remainder of the video. Time interval: 10 min (time: h:min:s; 7 fps). Scale bar: 10 µm. Accompanies Fig. 3 A.

Video 9. **Mitosis within monolayer of MDCK cells expressing GFP-vinculin and H2B-mCherry under confinement and following release of confinement.** Top: Schematic diagram showing the method of cellular confinement, in which MDCK cells are confined in height by a polydimethylsiloxane (PDMS)-coated glass slide to prevent mitotic cell rounding, and subsequently released from confinement. Bottom: time-lapse confocal imaging (z-projections) of monolayer of MDCK cells expressing GFP-vinculin (grays) and H2B-mCherry (cyan) during the different stages of confinement (indicated by asterisk in the diagram). Time interval: 3 min (confined) or 5 min (after release; time: h:min:s; 12 fps). Scale bar: 10 µm. Accompanies Fig. 3 C.

Video 10. **Z-stack of a mosaic MDCK cell monolayer with cells expressing either GFP-vinculin or mScarlet-vinculin.** Individual z-slices of a confocal image (Fig. 5 A) of a mosaic MDCK cell monolayer with cells expressing either GFP-vinculin (green) or mScarlet-vinculin (magenta). Z-interval = 0.5 µm (3 fps). Scale bar: 10 µm.